Daily weather types in February-June (1979-2016) and temperature variations in tropical North Africa

Vincent Moron, Boutheina Oueslati, Benjamin Pohl, Serge Janicot

Daily Weather Types in February–June (1979–2016) and Temperature Variations in Tropical North Africa

VINCENT MORON

Aix-Marseille University, CNRS/IRD/Collège de France/Centre de Recherche et d'Enseignement des Géosciences de l'Environnement, UM 34, Aix en Provence, France

BOUTHEINA OUESLATI AND BENJAMIN POHL

Centre de Recherches de Climatologie, UMR 6282 Biogéosciences, CNRS/Université de Bourgogne Franche-Comté, Dijon, France

SERGE JANICOT

Laboratoire d'Océanographie et du Climat, Sorbonne Universités, UPMC-IRD-CNRS-MNHN, UMR 7159, Paris, France

ABSTRACT

This study investigates to what extent weather types (WTs) computed over tropical North Africa and the tropical North Atlantic Ocean (40°W–40°E, 0°–30°N) are relevant for documenting intraseasonal and interannual temperature variability in tropical North Africa (west of 37°E, 2°–27°N). Nine WTs are extracted by using clustering analysis of the daily anomalies of sea level pressure and low-level 925-hPa winds from two reanalyses (NCEP–DOE and ERA-Interim) from 1979 to 2016. The analyses are carried out separately for February–March and for April–June, when temperatures reach their annual peak across most of the region. The WT patterns mix the effects of different multiscale phenomena, including the extratropical Rossby waves that travel on the northern edge of the domain (and are partly related to the North Atlantic Oscillation), the Madden–Julian oscillation, and Kelvin waves in the subequatorial zone. For each WT, warm (cold) minimum (TN) and maximum (TX) daily temperature anomalies tend to be systematically located east of cyclonic (anticyclonic) low-level circulation anomalies associated with the WT patterns. By modulating the greenhouse effect, the water vapor anomalies exert a major influence, leading to warm (cold) TX and TN anomalies associated with moister (drier) air, through advection from the tropical Atlantic or equatorial latitudes (the Sahara or northern latitudes) toward tropical North Africa. WTs are also useful for monitoring interannual variability of TX/TN anomalies mostly north of 10°N in February–March, even if they greatly underestimate the long-term warming trend. Most WTs significantly raise or lower the probability of regional-scale heat peaks, defined as the crossing of the 90th percentile of daily TX or TN.

1. Introduction

Tropical North Africa (the landmass west of 37°E, 2°–27°N) is among the inhabited regions of the world that regularly experience regularly diurnal temperatures of ≥40–45°C, especially during the boreal late winter and spring (February–June) (Moron et al. 2016b). The recent climatic warming in this region has been particularly intense (Lavaysse 2015; Cook and Vizy 2015). Anticipating and forecasting heat waves (HWs) is thus of crucial importance for West Africa and is a primary public-health issue because of the relationship between HWs and morbidity (Oudim Aström et al. 2011). Previous studies (Fontaine et al. 2013; Moron et al. 2016b; Oueslati et al. 2017) pointed out strong positive trends of maximum (TX) and minimum (TN) daily temperatures from at least the 1960s, as observed almost worldwide (Stocker et al. 2013), that are partly related to the increase in anthropogenic greenhouse gases. Moron et al. (2016b) and Oueslati et al. (2017) also show that El Niño–Southern Oscillation (ENSO) provides some interannual variability, with warm ENSO events leading to warm anomalies across tropical North Africa. Oueslati et al. (2017) also emphasize the primary role of the greenhouse effect enhancing the downward longwave radiation in the HWs detected during April–June 1979–2014 across the Sahel. This increased

greenhouse effect is mostly associated with the anomalous advection of moisture from the tropical North Atlantic Ocean and the equatorial Atlantic. In this paper, we investigate to what extent such temperature variability over tropical North Africa is embedded in regional-scale atmospheric circulation-anomaly patterns. This issue is explored through weather types (WTs) defined from a cluster analysis. Cluster analysis is a multivariate statistical technique that is based on the propensity of a collection of events [here, the daily atmospheric patterns from sea level pressure (SLP) and low-level 925-hPa wind anomalies around tropical North Africa] to group together into a small number of representative states (i.e., the WTs) according to a criterion of similarity (Cassou et al. 2004; Fereday et al. 2008). Our main goal is to analyze the WT characteristics and their relationships with TX/TN anomalies (including warm extremes) during the warmest season of the year across tropical North Africa.

Previous studies used WTs to diagnose and describe multiple flow regimes (Mo and Ghil 1988; Vautard and Legras 1988; Vautard 1990; Cheng and Wallace 1993; Michelangeli et al. 1995; Ghil and Robertson 2002; Fereday et al. 2008) and associated hemispheric- and regional-scale persistent and recurrent atmospheric patterns. WTs have often been adopted across the extratropical zone, mostly during winter, at either zonal scale or regional scale as over the North Atlantic and adjacent continents (Mo and Ghil 1988; Vautard and Legras 1988; Vautard 1990; Cheng and Wallace 1993; Michelangeli et al. 1995; Moron and Plaut 2003; Cassou 2008; Fereday et al. 2008). The WT framework has less often been used in the tropics (Pohl et al. 2005; Moron et al. 2008; Fauchereau et al. 2009; Moron et al. 2015, 2016a) and outside the wintertime season (Cassou et al. 2005). It is applied here to an area around tropical North Africa (40°W–40°E, 0°–30°N) in February–June. WTs are defined here using a dynamic clustering algorithm (i.e., k-means clustering) applied to the leading principal components (PCs) of daily low-level 925-hPa winds and SLP anomalies around tropical North Africa. WTs therefore correspond to the clusters' centroids, which are the time averages of daily atmospheric states belonging to a cluster. WTs thus provide a discrete and finite coarse-grained view of the continuous low-level atmospheric circulation (Michelangeli et al. 1995; Ghil and Robertson 2002; Fereday et al. 2008; Moron et al. 2015). From a statistical perspective, WTs correspond to high concentrations of daily atmospheric states in the phase subspace of atmospheric circulation spanned by the leading PCs. Within that context, WTs are not only quasi-stationary, persistent, and recurrent regional-scale atmospheric states, but they also provide snapshots of traveling waves. Moreover, WTs can be used to describe

the modulation of temperature or rainfall anomalies, including extreme events (Cassou et al. 2005; Roller et al. 2016).

The annual thermal peak across tropical North Africa is associated with increased incoming solar radiation around the northern solstice combined with desiccated soils just before the first (over Guinean latitudes) and the main (over Sudanian and Sahelian belts) rainy seasons (Guichard et al. 2009; Moron et al. 2016b; Oueslati et al. 2017; Barbier et al. 2018). The mean monthly atmospheric circulation over the tropical North Atlantic and tropical North Africa from February to June (Fig. 1) is dominated by two main centers of action: 1) the near-permanent Azores high (AH) and 2) the intertropical front (ITF), approximately defined as the surface limit between the northeastern trade winds (i.e., harmattan across Africa) and the southwestern-monsoon low-level flow (Sultan and Janicot 2003). The AH is extended by seasonal high pressure over tropical North Africa (sometimes referred to as the Libyan anticyclone) in February–March. The ITF is shifted northward of the main axis of the intertropical convergence zone (ITCZ) associated with deep convection and rainfall (Sultan and Janicot 2003; Nicholson 2009; Mera et al. 2014). The axis of the low pressure area across tropical North Africa is zonal and weak (1007–1009 hPa on average) and is located near 10°N in February (Fig. 1a). The ITF intensifies in March (Fig. 1b) and shifts slowly northward almost as far as 15°–18°N in May–June (Figs. 1d,e) with an extension toward the Saharan heat low (Lavaysse et al. 2009; Chauvin et al. 2010) near 25°N and 0° longitude from April (Fig. 1c). North of the ITF, the northerlies are stronger over the western Sahara and Sahel, in association with the intensifying AH, while pressure fails over the Sahara, especially from April, but also over the Arabian Peninsula as a result of the deepening of the heat low associated with the Asian monsoon. The broad-scale seasonal changes in the mean atmospheric state, mostly the establishment and intensification of the African continental heat low and the progressive slowdown of the extratropical westerlies on the northern edge of our domain, lead us to produce separate analyses for February–March (FM) and April–June (AMJ). Note that the highest mean TXs are observed around 11°–12°N in FM and 16°–17°N in AMJ, whereas the highest mean TNs are invariably observed over the equatorial Atlantic (Figs. 10 and 11; described in more detail below in section 4b).

This paper is organized as follows. Section 2 presents the datasets used in the study. Section 3 describes the WT characteristics in terms of spatial patterns, transitions, and recurrence. Section 4 analyzes the modulation of TX/TN anomalies and those of three terms of the
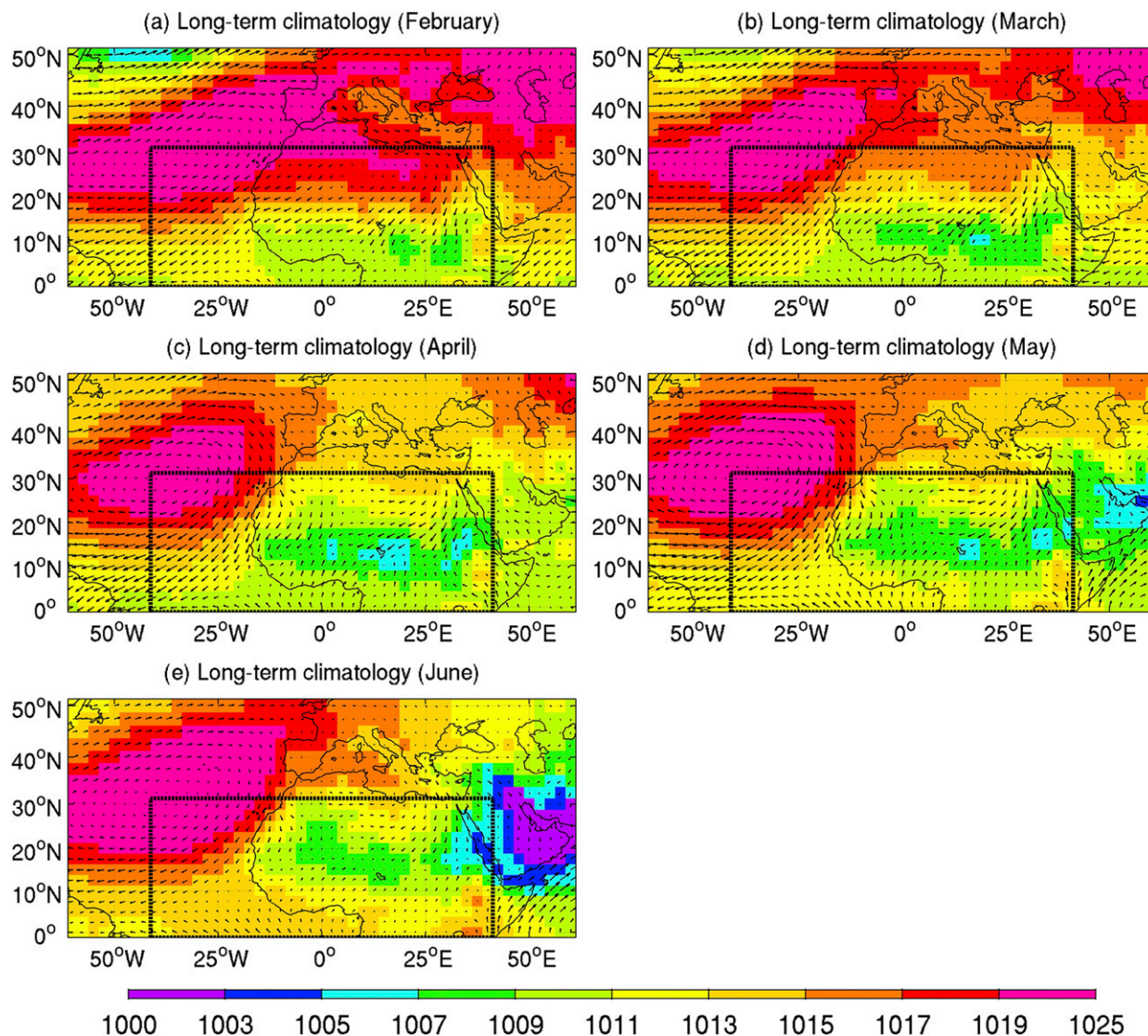
FIG. 1. Mean monthly mean SLP (shading; hPa) and low-level 925-hPa winds (vectors). The long-term mean is computed from the concatenation of R2 and ERA daily fields during the 1979–2016 period. The box shows the area used in the *k*-means clustering of daily anomalies of SLP and low-level 925-hPa winds.

energy budget (defined in section 2a) by the WTs. Section 5 uses the WT sequences to reconstruct the interannual variations of seasonal TX and TN anomalies and the extreme heat peaks in daily TX and TN. Section 6 summarizes the main results.

2. Data

a. Reanalyzed atmospheric variables

Atmospheric data were obtained from the NCEP–DOE AMIP-II reanalysis (R2; Kanamitsu et al. 2002) and ERA-Interim (ERA; Dee et al. 2011). Daily sea level pressure (SLP) and low-level 925-hPa winds were extracted from 1 February to 30 June 1979–2016. The low-level 925-hPa winds are considered to account for variability of the tropical atmosphere where the SLP variations are relatively weak. The daily data are standardized to 0 mean and unit variance by removing the climatological daily mean and dividing by the climatological daily standard deviation. Daily TX and TN from R2 and ERA are used to check results obtained with stations and gridded temperatures (see below). Radiative fluxes [i.e., the greenhouse effect at the surface (GHE; defined as the downward longwave radiation at the surface) and the surface net shortwave radiation (SWR)] and the vertically integrated moisture convergence (MoistConv) are also computed from ERA daily fluxes (Oueslati et al. 2017).

b. The North Atlantic Oscillation (NAO) and Madden–Julian oscillation (MJO)

We analyzed the modulation of the WT occurrence by the main regional-scale extratropical mode of variation across the North Atlantic (i.e., the NAO) and the main intraseasonal mode of variation across the tropics (i.e., the MJO). The daily index of the NAO was obtained online (ftp://ftp.cdc.noaa.gov/Public/gbates/teleconn/nao.reanalysis.t10trunc.1948-present.txt). The NAO is based on centers of action of 500-hPa geopotential height anomalies from the NCEP–NCAR reanalysis dataset (R1; Kalnay et al. 1996). The averaged region 55°–70°N and 70°–10°W, corresponding to the usual location of the subpolar Icelandic low pressure center, is subtracted from 35°–45°N and 70°–10°W, corresponding to the usual location of the center or the northern margins of the subtropical AH. The 1981–2010 period was used as climatological normal. Before computing these indices, the 500-hPa height fields are spectrally truncated to total wavenumber 10 to emphasize large-scale aspects of the NAO-related teleconnection. Daily values are extracted for FM and AMJ and standardized to 0 mean and unit variance over the 1979–2016 period.

The MJO index comes from Wheeler and Hendon (2004) and discretizes the MJO cycle into nine categories, including eight active phases corresponding to the approximate longitudes of the enhanced convective signal close to the equator (the Indian Ocean for phases 2 and 3, the "Maritime Continent" for phases 4 and 5, the western Pacific Ocean for phases 6 and 7, and the Western Hemisphere and Africa for phases 8 and 1). An additional category refers to weak MJO activity.

c. Observed maximum and minimum temperatures

Daily TX and TN are analyzed through two databases. The first results from the concatenation, checking, and filling of 90 stations that are mostly from the Global Summary of the Day (GSOD) and the daily Global Historical Climatology Network datasets from 1979 to 2014 (Moron et al. 2016b). The second is the 1°-grid daily temperature dataset from the Berkeley Earth group for 1979–2013 (http://berkeleyearth.org/data/).

3. Extraction and characteristics of weather types

a. Method

We applied the k-means partitioning algorithm (Cheng and Wallace 1993; Michelangeli et al. 1995) to standardized anomalies of daily SLP and zonal and meridional components of the low-level 925-hPa winds in the boreal late winter (FM) and spring (AMJ) seasons over the domain 40°W–40°E and 0°–30°N. The standardized anomalies of daily SLP and zonal and meridional components of low-level 925-hPa winds were first preprocessed using an empirical orthogonal function (EOF) that retains 75% of the total variance in the concatenated matrix. The EOF prefiltering removes the smallest spatial scales but also the shortest temporal scales. Clustering is applied to the leading PCs from 2 to 10 clusters with 1000 random seeds. The solution achieving the largest mean pattern correlation with the other 999 seeds is retained as the final clustering. The resulting WTs should be interpreted against the climatological mean state (Fig. 1). "Robust" WTs are extracted from the concatenated matrix including R2 and ERA, that is, the 86% and 78% of days in FM and AMJ, respectively, that are assigned to the same WT in both reanalyses. Days belonging to different WTs in R2 and ERA correspond either to atmospheric states near the edges of the subspace defined by the clusters or to less certain, model-dependent configurations, which are presumably poorly constrained by data assimilation. Hence, they are omitted from the following analyses.

b. The choice of the number of clusters

The number of clusters (i.e., k) needs to be set first in a dynamic clustering as k means. We consider here two complementary approaches for finding an optimal ad hoc value for k between 2 and 10. The first approach involves the degree of sensitivity of the final clustering versus the random seeds (1000 random seeds are used for each value of k), using the classifiability index (CI; Michelangeli et al. 1995) as modified by Roller et al. (2016). The optimal solution is reached when CI = 1, meaning that the clustering is fully insensitive to the random seeds. Figures 2a and 2b show the CI with the one-sided 95% level of significance estimated from 100 simulations of red noise having the same one-order autocorrelation as the selected principal components. The CI is over the 95% level of significance for k = 2, 3, 7, and 9 clusters in FM (Fig. 2a) and for k = 2, 3, 5, 6, and 9 clusters in AMJ (Fig. 2b). The second approach involves the degree of discrimination of TX/TN anomalies according to the WTs, associated with the centroids of clusters. The optimal solution is reached when the spatially averaged mean absolute TX and TN anomalies are maximized, usually for k = 9 (Figs. 2c–f).

The most parsimonious clustering solution (i.e., k = 2) mostly opposes "zonal" and "blocking" atmospheric circulations on the subtropical northern margin of the domain (not shown) and does not provide a sound discretization of TX and TN anomalies across tropical North Africa, especially in AMJ (Figs. 2d,f). Considering a larger number of clusters obviously further discretizes the atmospheric circulation, including snapshots of traveling "small" waves, including opposite low-level atmospheric
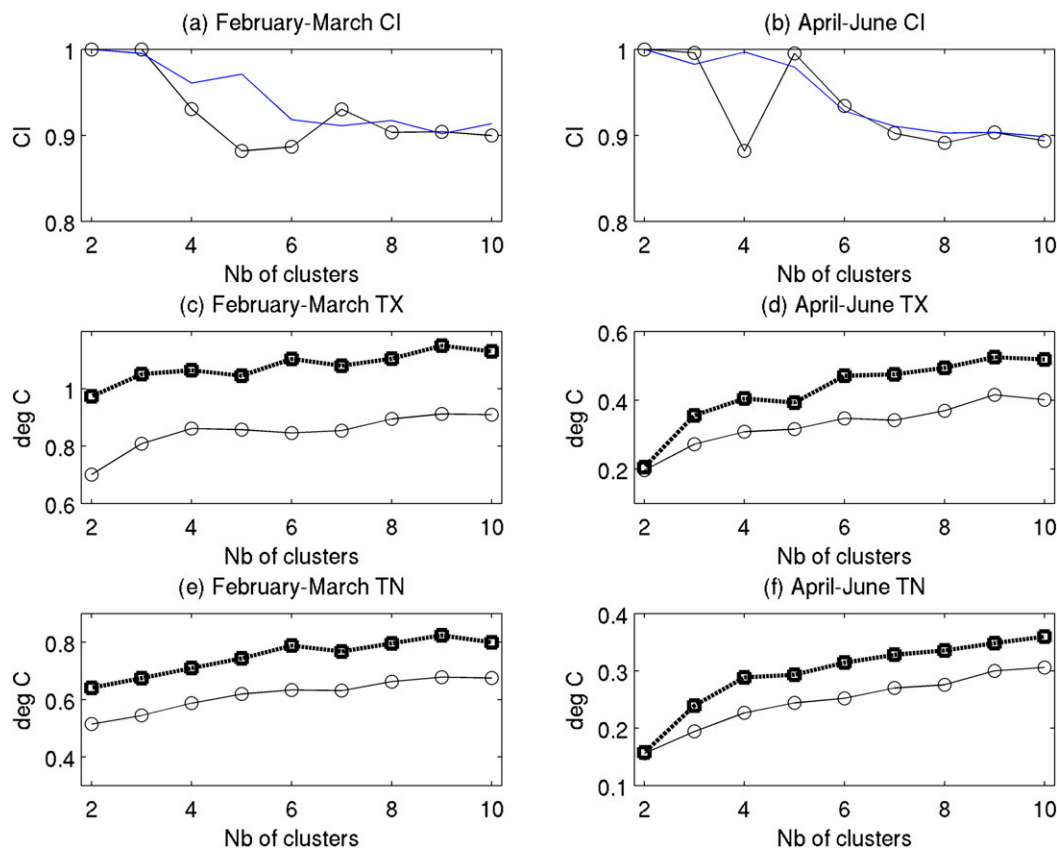
FIG. 2. Classifiability index (black line with open circles) corresponding to the *k*-means clustering of the leading PCs explaining 75% of variance for the (a) FM and (b) AMJ standardized anomalies of daily SLP and 925-hPa winds in the 40°W–40°E and 0°–30°N domain, by number of clusters. The blue line is the 95% level of significance estimated with 100 simulations of red noise having the same autocorrelation and same standard deviation as the leading PCs. Also shown are the mean absolute (c),(d) TX and (e),(f) TN anomalies associated with all clustering in (left) FM and (right) AMJ for the Berkeley Earth gridded dataset (thick line with open squares) and observed GSOD stations (thin line with open circles).

anomalies in the spatial window taken into account, and by definition it improves the discrimination of TX and TN anomalies (Figs. 2c–f). Even if a large number of clusters may subdivide the same atmospheric phenomena (such as extratropical eastward-propagating Rossby waves) into several snapshots, the partitioning into nine clusters is retained for both seasons since this solution 1) maximizes relationships with temperature as indicated in the previous paragraph, except for TN in AMJ (Fig. 2f), and 2) can be used to compare and contrast FM and AMJ using the same level of clustering. The sensitivity of some of the results to the number of clusters is discussed in section 5b.

c. WT patterns: General characteristics

The nine WTs (Fig. 3 for FM and Fig. 4 for AMJ) are shown as composites of the SLP and low-level 925-hPa wind daily standardized anomalies over a larger domain than the one used for clustering (shown as a rectangular

box in Figs. 3a and 4a). The local-scale and global-scale significances of SLP and wind anomalies are computed using 1000 random resamplings of the WT sequences. The WT sequences are randomly reshuffled by blocks of five consecutive days to consider the persistence over time of WTs (Fig. 5). The local significance is estimated for each variable through the rank of observed anomalies versus the PDF of anomalies from the 1000 reshuffled sequences. The overall significance is computed by comparing the observed area that is locally significant at significance level $p = 0.05$ with the ones in the 1000 random resamplings. Note that almost all of the composites shown in Figs. 3 and 4 (and also in Figs. 8–13, described below) are globally significant at least at the $p = 0.05$ level; that is, the observed surface locally significant at $p = 0.05$ is not reached by more than 5% of the random resamplings. The WTs are ordered from cold to warm anomalies on the basis of the mean extent
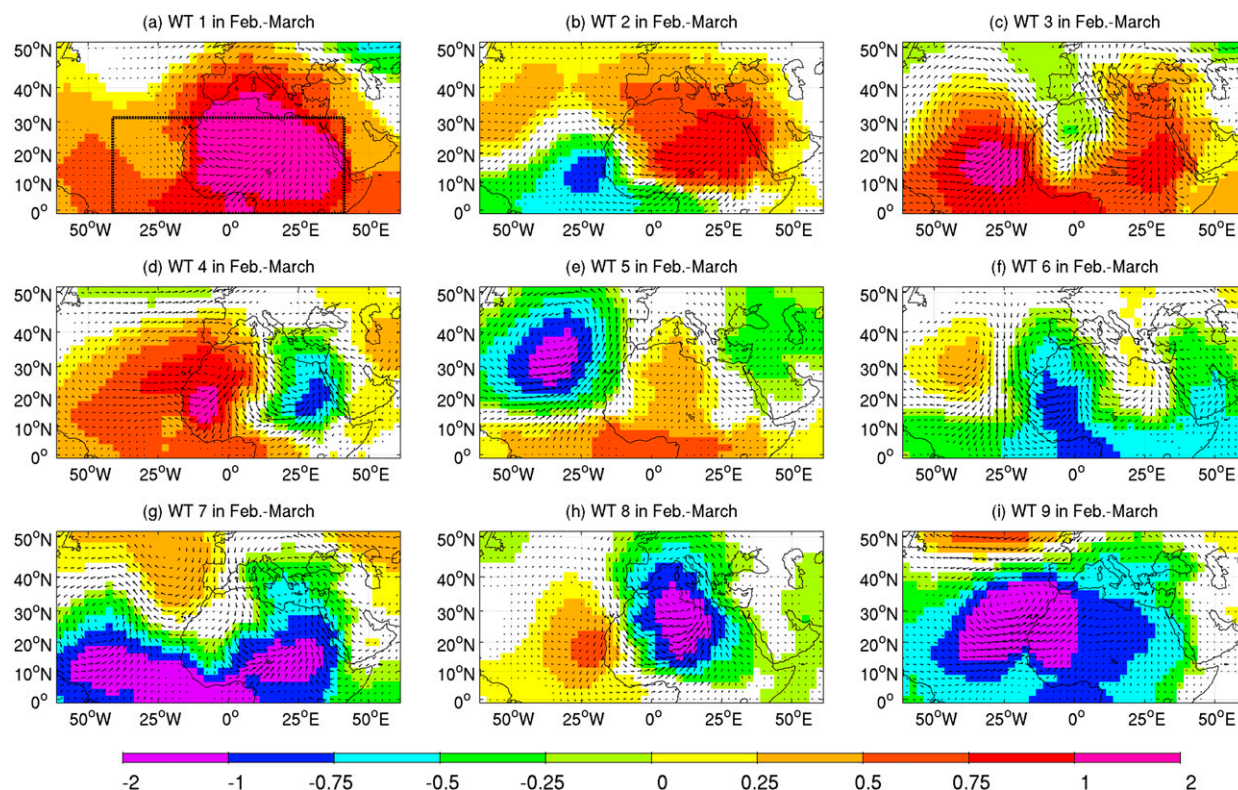
FIG. 3. Mean SLP (colors, in standard deviations) and 925-hPa wind (vectors) standardized anomalies associated with the nine WTs in February–March. Only days belonging to the same cluster in R2 and ERA are used in the mean composite, and only significant anomalies (for winds, either the zonal or the meridional component) at the two-sided 95% level according to 1000 random resamplings of WT time series are displayed. The rectangular box in (a) delineates the area used to compute the WTs.

of positive TX and TN anomalies (from the Berkeley Earth dataset) spatially averaged across the region. Figure 5 shows the probability of transitions among the WTs. The transitions among the WTs are tested using random resamplings of WT sequences and counting the proportion (of a total of 1000 simulations) reaching the observed probability. The transitions are computed for seven lags; the first lag is from one day to the next and the last lag is from one day to one week after. The most robust transitions are self-transitions (i.e., the WT lasts for 2–8 consecutive days), which are frequently significant at all lags (Figs. 5a,b).

Last, for a better physical interpretation of the WTs, Figs. 6 and 7 show the anomalous frequency of each WT associated with two regional-scale extratropical and planetary-scale tropical modes of variation (i.e., the NAO and the MJO). These possible modulations of the WT occurrence by either the NAO or the MJO are completed by Figs. 8 and 9, which show their respective composite time series of mean SLP anomaly fields over a larger domain covering equatorial latitudes down to 25°S from 6 days before the start (i.e., the first day belonging to a given WT) to 2 days after the end (i.e., the last day

belonging to a given WT) of the WT sequences, independent of their lengths. As for Figs. 3 and 4, the SLP anomalies in Figs. 8 and 9 are expressed in terms of standardized values with respect to the standard deviation for each grid point, and their significance is computed similarly.

Two kinds of pressure anomaly and low-level wind patterns are combined in the WT composite patterns of Figs. 3, 4, 8, and 9. The first kind involves cases in which the high SLP anomalies of the same sign are located over the equatorial latitudes, are zonally oriented, and generally propagate eastward or are quasi stationary (Figs. 8 and 9). This pattern is consistent with either the MJO (Madden and Julian 1994; Zhang 2005) or faster Kelvin wave (Kiladis et al. 2009) patterns. Kamsu-Tamo et al. (2014) showed that such equatorial waves, coupled to the convection, are regularly recorded in March–June over the equatorial Atlantic, the Guinean coast, and central Africa, both at the synoptic (2–8 day) and intraseasonal (8–22 day) time scales. The second pattern presents cases in which the highest SLP and low-level 925-hPa wind anomalies are located over the northern subtropical latitudes; they are meridionally oriented and
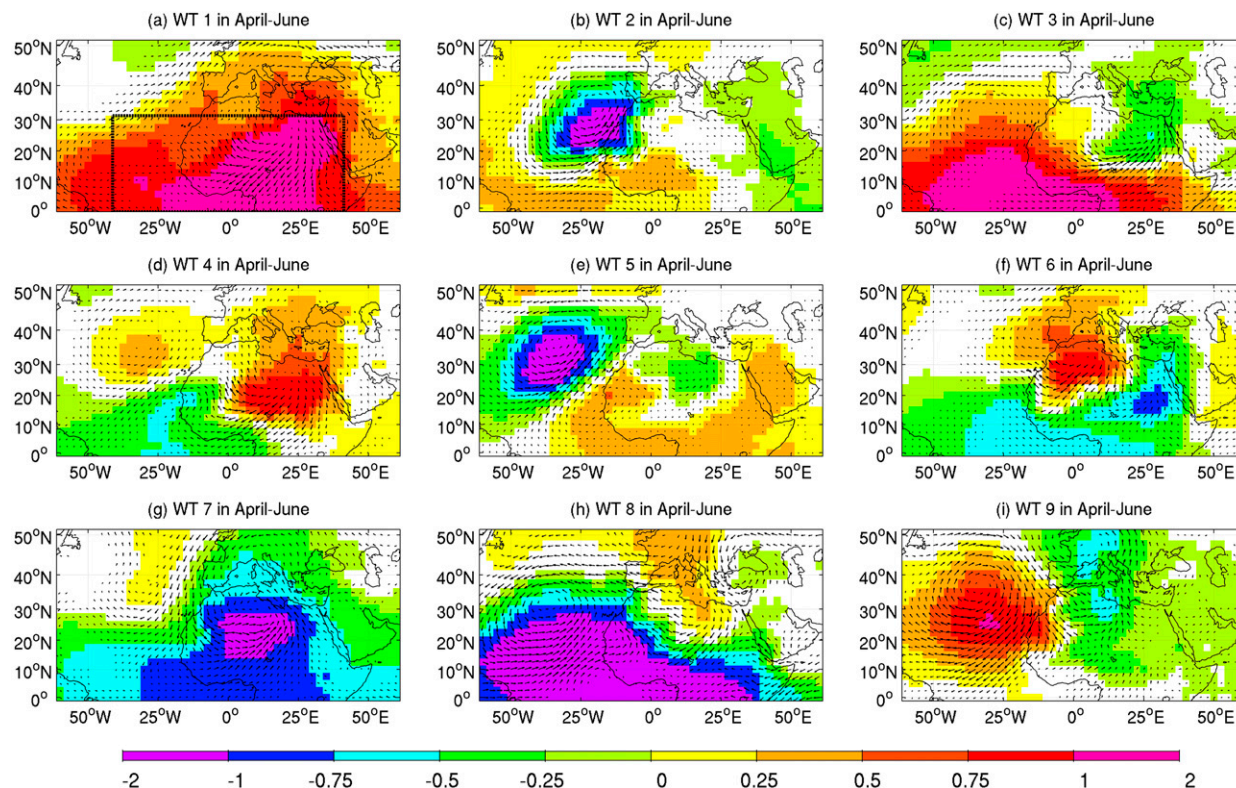
FIG. 4. As in Fig. 3, but for April–June WTs.

generally propagate eastward or are quasi stationary. Similar pressure patterns were found in the northern winter by Blackmon et al. (1984a), among many others, and were related to zonally oriented Rossby baroclinic wave trains near the jet streams with zonal wavenumbers 6 and 7 (wavelength of 6000 km) at the synoptic time scale (2.5–6 days). At the intraseasonal time scale (10–30 days), such pressure patterns are still present. They originate from the jet-entrance regions and cross the jet streams as they curve southeastward into the tropics, associated with a Rossby wave dispersion (Blackmon et al. 1984b). Chauvin et al. (2010) showed that such intraseasonal patterns are present during the northern summer over North Africa.

d. WT patterns and transitions in February–March

In FM, there are two families of interconnected WTs:

1) WTs 1–4 are associated with mostly positive SLP anomalies across most of tropical North Africa and are favored during the positive phase of the NAO, especially WTs 1 and 4 (Figs. 3a–d and 6a).
2) WTs 5–9 are associated with mostly negative SLP anomalies across most of tropical North Africa and are favored during the negative phase of the NAO, especially WTs 5 and 9 (Figs. 3e–i and 6a).

Neither family (i.e., WTs 1–4 on one hand and WTs 5–9 on the other hand) is connected at a scale of 7 days, except from WT 8 to WT 4 and weakly from WT 5 to WT 1 (Fig. 5a).

One can also notice opposing WTs between the two families, such as WT 3 (Fig. 3c) versus WT 7 (Fig. 3g), WT 1 (Fig. 3a) versus WT 9 (Fig. 3i), and, to some extent, WT 2 (Fig. 3b) versus WT 8 (Fig. 3h) and WT 4 (Fig. 3d) versus WT 5 (Fig. 3e). WTs 3 and 7 have the closest patterns to that of a Kelvin wave, that is, an SLP anomaly that is mostly symmetric with the equator and moving eastward, with some northward extension at the location of the ridges of the Azores and Libyan anticyclones (Fig. 8). Both are significantly modulated by the MJO (Fig. 6b), with WT 3 and WT 7 occurring more and less frequently, respectively, than by chance when the main convective center is located over the Maritime Continent (Fig. 6b). WT 6 (Fig. 3f) has a pressure anomaly pattern that is similar to the WT 7 pattern (Fig. 3g), but with weaker anomalies. WTs 1 and 9 display a quasi-stationary and extended modulation of pressure centered over the northwestern coast of Africa (Fig. 8). They are both strongly (and inversely) modulated by the MJO (Fig. 6b). WT 8 is similar to an extratropical Rossby wave train characterized by a dipolar pattern of a pressure anomaly of
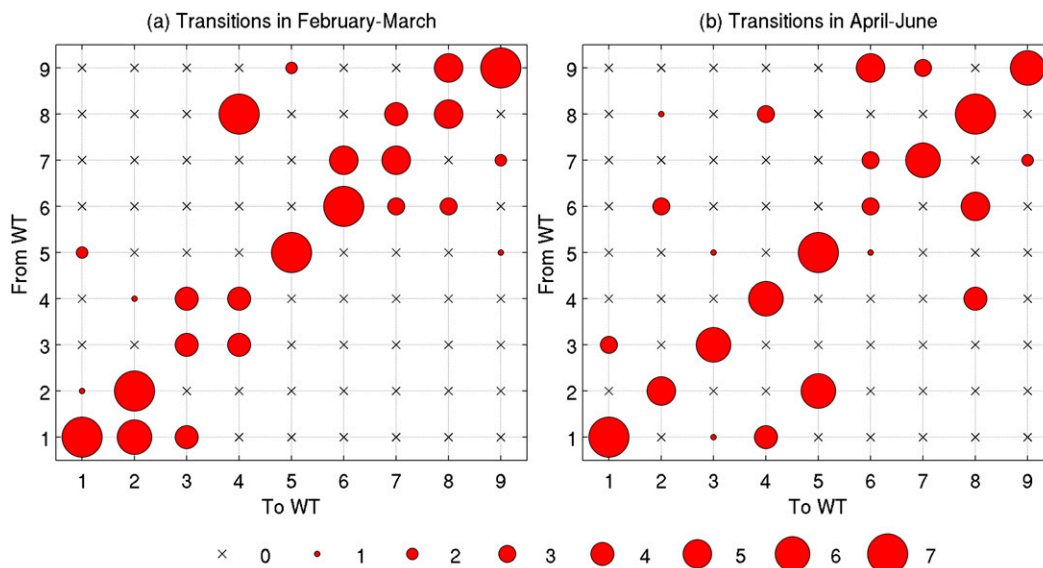
FIG. 5. Probability of transitions from WT (in rows) to WT (in columns) during (a) FM and (b) AMJ. The size of the red circles is proportional to the number of transitions (ranging over from one day to the next to one day to the seventh day thereafter) that occur significantly more often than they would by chance at the one-sided 95% level according to 1000 random resamplings of WT time series. A cross means that no transition reaches this level of significance for all lags.

short wavelength located over the northern subtropical latitudes and usually traveling eastward, as described by Blackmon et al. (1984b) among many others (Fig. 8), and WT 4 shows some similarities (Fig. 8). WT 5 displays a quasi-stationary Rossby wave pattern and is also mixed with some pressure signals over the equator (Fig. 8). WT 2 has an organization of pressure anomalies that similar to that of WT 5 in terms of dipolar pressure anomalies between the equator and the subtropical latitudes, but with the opposite sign.

Hence, the two families (WTs 1–4 on the one hand and WTs 5–9 on the other hand) include subequatorial MJO/ Kelvin wave patterns to extratropical Rossby wave trains and intermediate patterns. In that context, the WTs may be viewed not necessarily as dynamic attractors of atmospheric circulation, but rather as statistical combinations of different phenomena and scales, that is, primarily extratropical Rossby waves with the fingerprints of subequatorial MJO and Kelvin waves at intraseasonal and shorter time scales. Some similarity among several WTs is also inevitable as a result of the mixing of traveling waves in the WTs, since similar WTs may be close snapshots of a similar mode of variation.

e. WT patterns and transitions in April–June

Similar results hold for AMJ (Figs. 4, 5b, 7, and 9). The transition matrix (Fig. 5b) highlights three families of interconnected WTs:

1) WT 1 (Fig. 4a), WT 3 (Fig. 4c), and WT 4 (Fig. 4d), with mostly positive SLP anomalies at least across tropical North Africa and extending toward the equatorial latitudes, are similar to a Kelvin wave pattern (except WT 4, which has less-extended negative pressure anomalies; see Fig. 9). Consistent with these patterns, WT 3 and, to a lesser extent, WT 1 appear to be highly modulated by the MJO phases (Fig. 7b).
2) WT 2 (Fig. 4b) and WT 5 (Fig. 4e), with the highest negative SLP anomalies over the subtropical latitudes of the North Atlantic, seem to be linked to Rossby wave trains (Fig. 9). WT 5 is the sole WT in AMJ that is closely related to the NAO phases (Fig. 7a).
3) WTs 6–9 (Figs. 4f–i), with mostly negative SLP anomalies extended over the equatorial latitudes, are similar to a Kelvin wave pattern with some northward extension [except for WT 9 (Fig. 4i), which depicts a Rossby wave train over the subtropical latitudes]. Nevertheless, these WTs are only weakly modulated by the NAO (Fig. 7a). WTs 6 and 8 are strongly and similarly modulated by the MJO and occur more frequently when the cyclonic pole of the MJO is close to Africa (i.e., during phases 8 and 1; see Fig. 7b).

These three families are loosely connected at a scale of 7 days (Fig. 5b), except from WT 4 to WT 8 (and vice
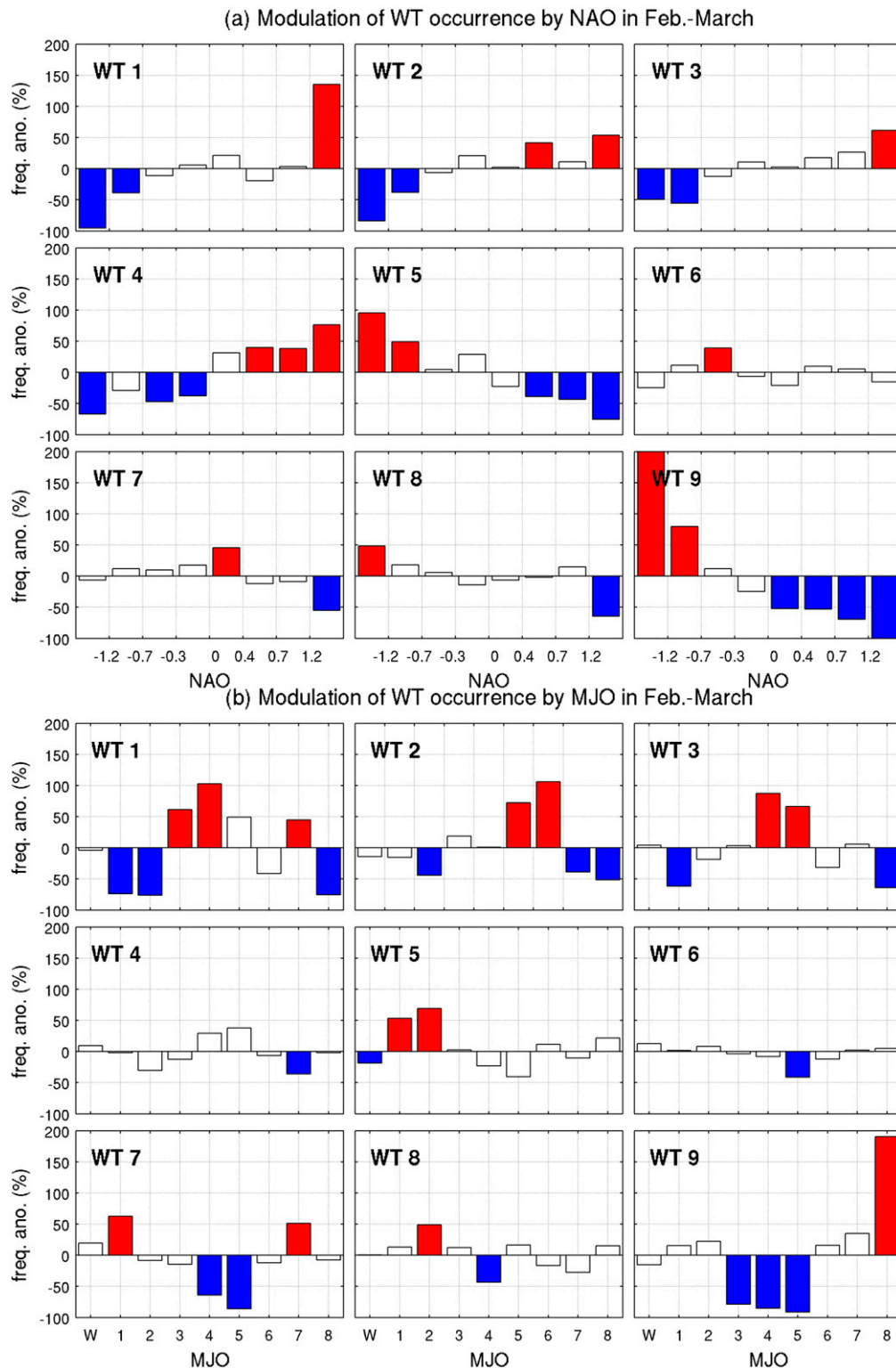
FIG. 6. (a) Anomalous frequency (vs expected frequency by chance; %) of the occurrence of the nine WTs in February–March according to the daily NAO index. Blue and red bars indicate significant negative and positive anomalies, respectively, at the two-sided 95% level according to 1000 random reshufflings of the WT time series. (b) As in (a), but for the modulation related to the planetary-scale MJO. The "W" in the x-axis labels in (b) indicates unclassified MJO days resulting from real-time multivariate MJO series 1 and 2 (RMM1 and RMM2, respectively) indices that are close to 0 (Wheeler and Hendon 2004).
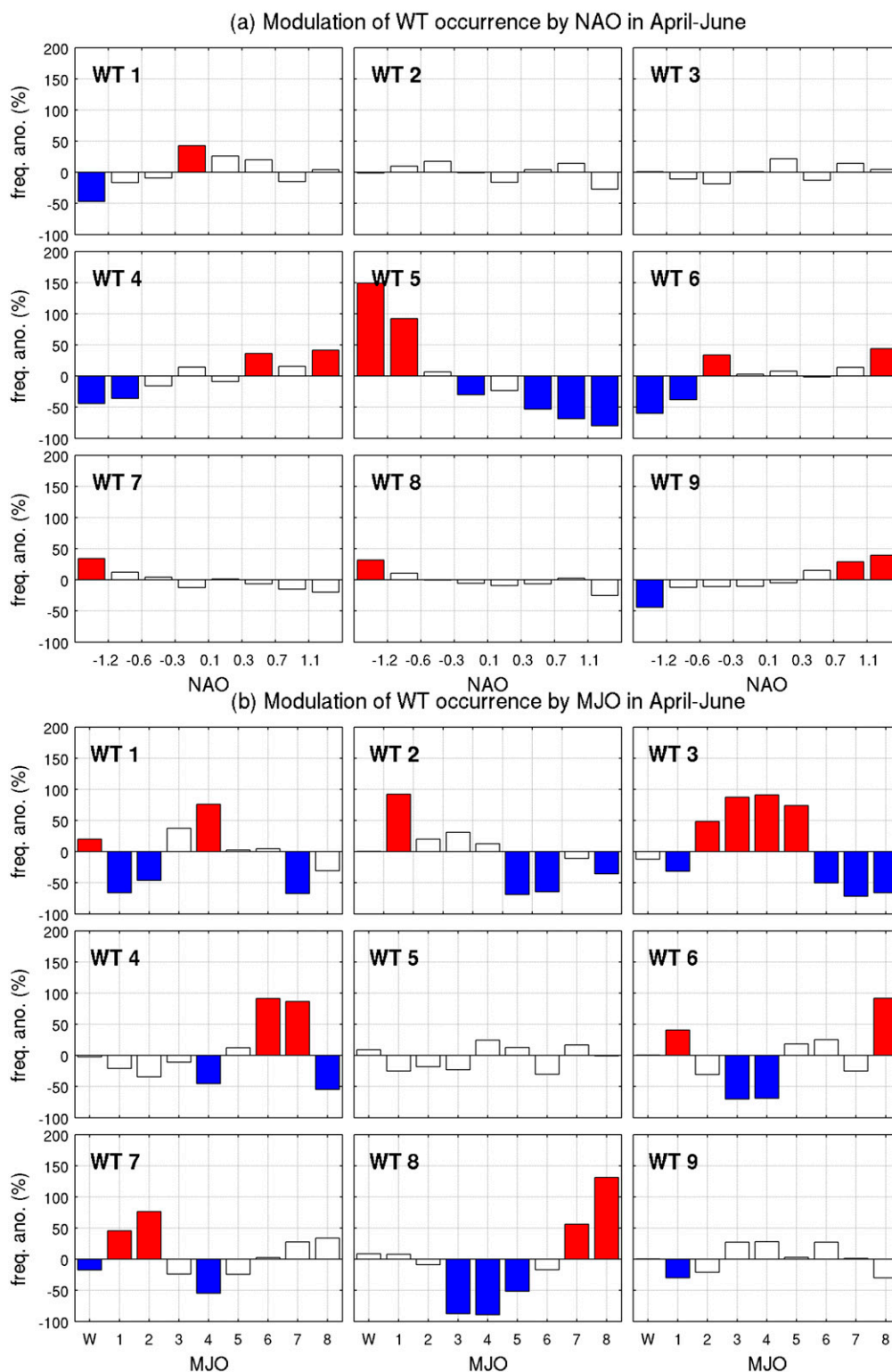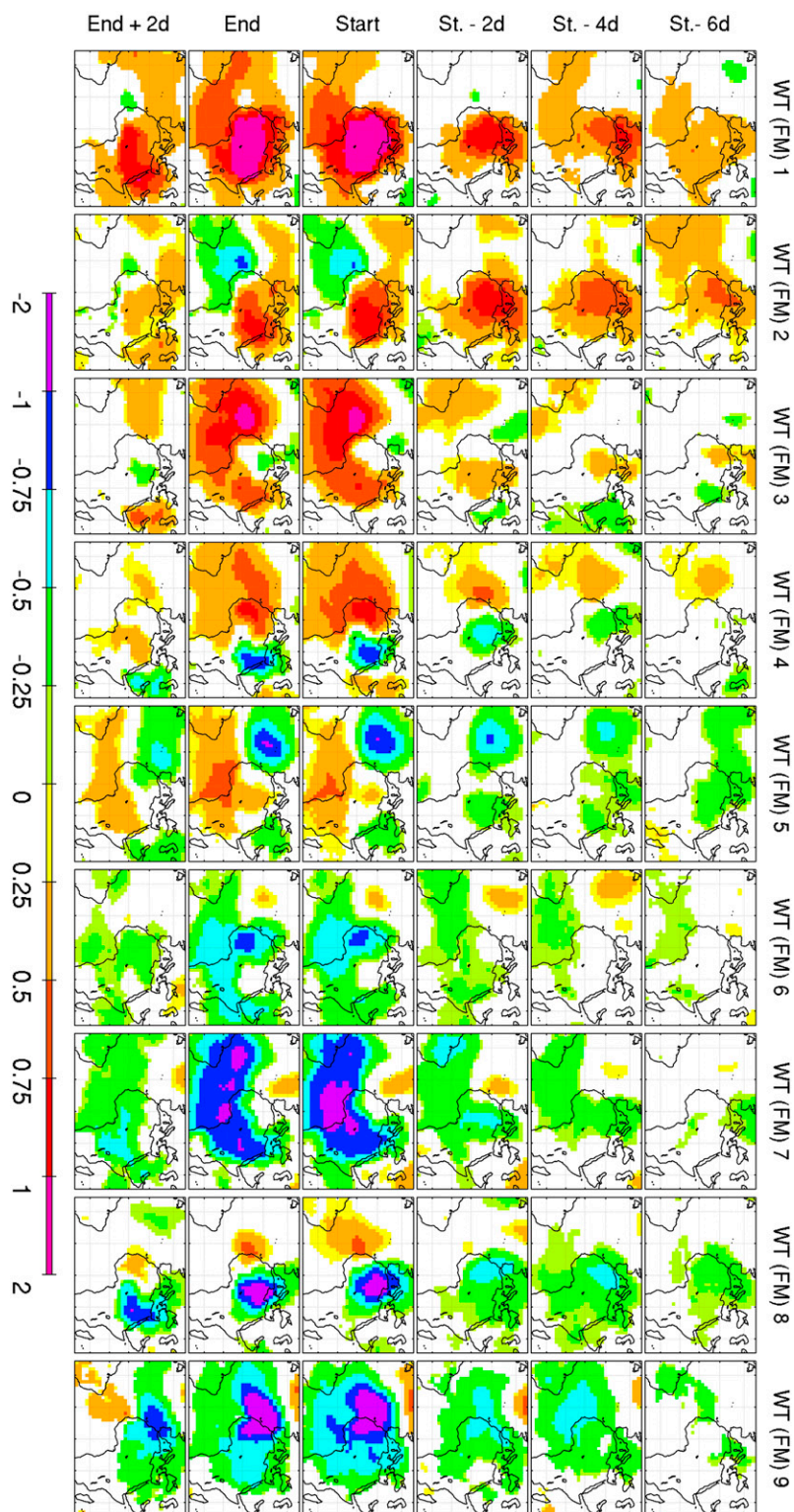
FIG. 7. As in Fig. 6, but for AMJ.

FIG. 8. Mean SLP anomalies (in standard deviations) associated with the nine weather types in February–March keyed to the first (labeled Start) and last (labeled End) days of spells with a time step of 2 days from 6 days before the start to 2 days after the end of a sequence. Only significant anomalies at the two-sided 95% level according to 1000 random resamplings of WT time series are displayed.
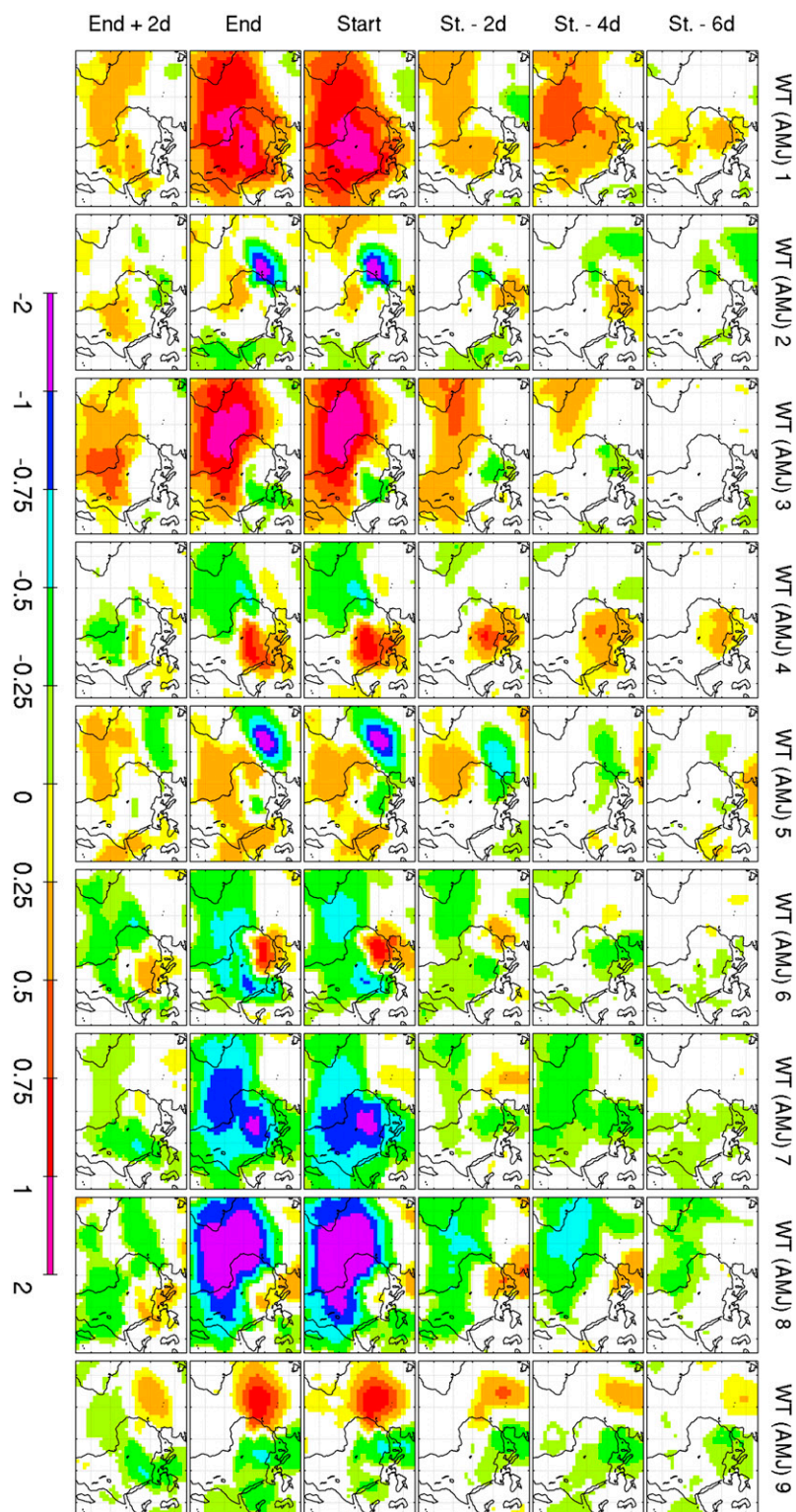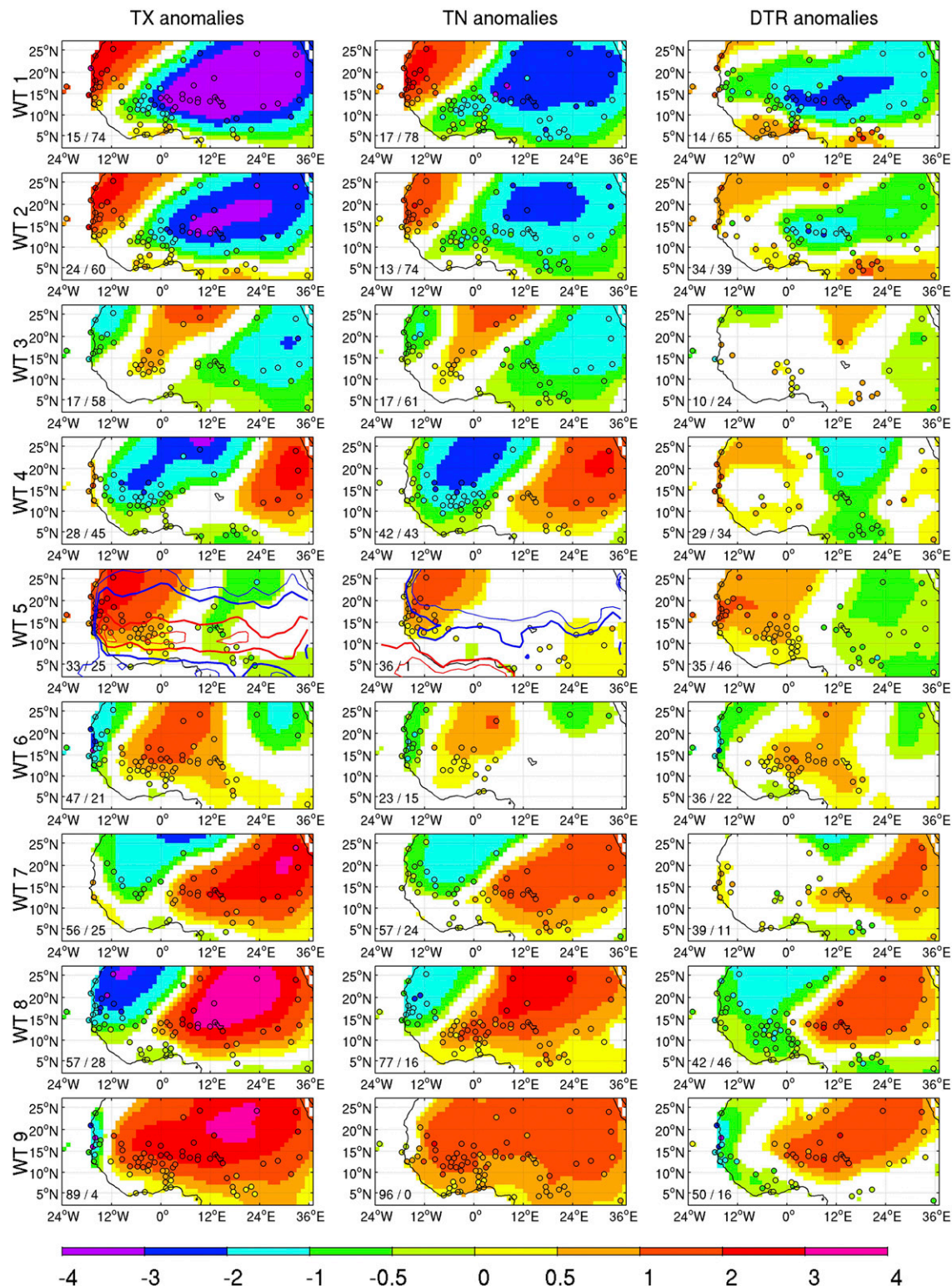
FIG. 9. As in Fig. 8, but for AMJ.

FIG. 10. Mean (left) maximum temperature, (center) minimum temperature, and (right) diurnal temperature range anomalies (°C) in the 90-station network (colored circles) and the gridded Berkeley Earth dataset (shades) associated with the nine WTs during February–March. Only significant anomalies at the two-sided 95% level according to 1000 random reshufflings of WT time series are displayed. The numbers indicated in the bottom-left corner of each panel are the percentages of the whole domain covered by significant positive and negative thermal anomalies (in the Berkeley Earth dataset). In the TX panel corresponding to WT 5, the contours delineate the climatological TX means of 301 K (thin blue contour), 304 K (thick blue contour), 311 K (thick red contour), and 314 K (thin red contour). In the TN panel corresponding to WT 5, the contours delineate the climatological TN means of 287 K (thin blue contour), 290 K (thick blue contour), 297 K (thick red contour), and 300 K (thin red contour).

versa), and weakly connected from WT 6 to WT 2. Then, the WT 6–9 family is the only one connected to the other two. As for FM, opposing WTs can be observed such as WT 1 (Fig. 4a) versus WT 8 (Fig. 4h), or WT 2 (Fig. 4b) versus WT 9 (Fig. 4i). In AMJ, the spells tend to be less persistent than in FM (not shown).

4. Relationships between WT and temperature/ thermodynamic processes

a. Introduction

The relationships between WT occurrence and the regional-scale temperature anomalies are first analyzed through the mean WT composite anomalies of TX, TN, and diurnal temperature range (DTR) for FM (Fig. 10) and AMJ (Fig. 11). Together with atmospheric circulation patterns, the local thermodynamic processes have a crucial effect on the temperature anomalies by modifying the surface energy budget (Oueslati et al. 2017). In West Africa, the radiative processes including shortwave and downward longwave radiation at the surface are of great importance and are highly sensitive to the water vapor and cloud processes (Guichard et al. 2009; Oueslati et al. 2017). In particular, the downward longwave radiation at the surface results from the greenhouse effect of water vapor and midlevel clouds, with the former dominating the response (Oueslati et al. 2017). The latter study investigated the origin of the abundant water vapor within the atmosphere by computing MoistConv (defined in section 2a). They highlighted the crucial role played by the low-level convergence through the advection of water vapor from the tropical Atlantic Ocean and the Guinean coasts toward continental Africa. Figures 12 and 13 show the mean WT composite anomalies for the different contributions of the GHE, SWR, and MoistConv anomalies to the temperature anomalies stated above.

First, the patterns and amplitudes of the thermal anomalies fit well between the 90-station network and the gridded Berkeley Earth dataset, even for subtle patterns such as warm TX anomalies stretching along the coast between Ziguinchor, Senegal (12.55°N, 16.28°W), and Nouadhibou, Mauritania (20.93°N, 17.03°W), during WT 9 in FM (Fig. 10). There are also no large differences between the TX and TN anomaly patterns, although their amplitudes may differ, leading to contrasted DTR (Figs. 10 and 11). The TX and TN anomalies tend also to frequently switch from positive to negative values (and vice versa) between 10°W and 10°E on each side of a southwest–northeast transition sector with near-zero TX and TN anomalies

(Figs. 10 and 11), that is, between an "Atlantic" and a "continental" domain.

b. Relationships between WT and temperature/ thermodynamic processes in February–March

In FM, there is no WT associated with homogeneous cold TX or TN anomalies, whereas warm anomalies are widespread for WT 9 (Fig. 10) except for a narrow coastal strip restricted to Senegal and Mauritania where the TXs only are anomalously cold. The alternating positive and negative TX/TN anomalies (Fig. 10) are usually associated with anomalous southerly and northerly flows (Fig. 3). Thus, the negative TX/TN anomalies are usually located east and south (i.e., downstream if the basic flow is westerly) of positive SLP anomalies while the positive TX/TN anomalies are usually located west of the positive SLP anomalies. This suggests that the advection of anomalously moist/ dry air is the primary term relating the WTs and the thermal anomalies. It is obvious that the advection of warm/cold air also plays a role. The air coming from the coolest regions (i.e., the Sahara north of 20°N for TX and TN plus the Atlantic Ocean for TX only (see climatological TX and TN averages in the WT 5 panels of Fig. 10) tends to cool the regions crossed. On the contrary, the air coming from the warmest region (i.e., the equatorial Atlantic for TN and continental Africa) between roughly 8° and 18°N for TX (see climatological TX and TN averages in the WT 5 panels of Fig. 10) tends to warm up the regions crossed. The cold TX/TN anomalies are stronger when the anomalous northerly flow comes from the continent, as in WT 1 and WT 2 (Fig. 10), but also in WT 4 across the central Sahara and western Sahel, downstream of vigorous northerly anomalies between an intensified AH while the pressure is lower than usual from Egypt to central Africa (Fig. 3d).

The thermodynamic processes associated with the WTs (Fig. 12) confirm the very strong link between the TX/TN and GHE anomalies: positive (negative) TX/TN anomalies (Fig. 10) are related to positive (negative) GHE anomalies (Fig. 12). The spatial correlations between the composite TX/TN (Fig. 10) and the GHE anomalies (Fig. 12) are very high, especially for TN (Table 1). Positive anomalies of GHE are associated with abundant water vapor within the atmosphere, resulting from the larger moisture convergence toward the regions of positive thermal anomalies (Fig. 12, right column). Indeed, the pattern correlation between the GHE and the MoistConv anomalies is equal to 0.60, 0.58, 0.67, 0.56, 0.53, and 0.61 for WTs 3, 4, and 6–9, respectively. The relationships between the TX/TN and GHE anomalies are weaker for WT 9 (Figs. 10 and 12; Table 1). For
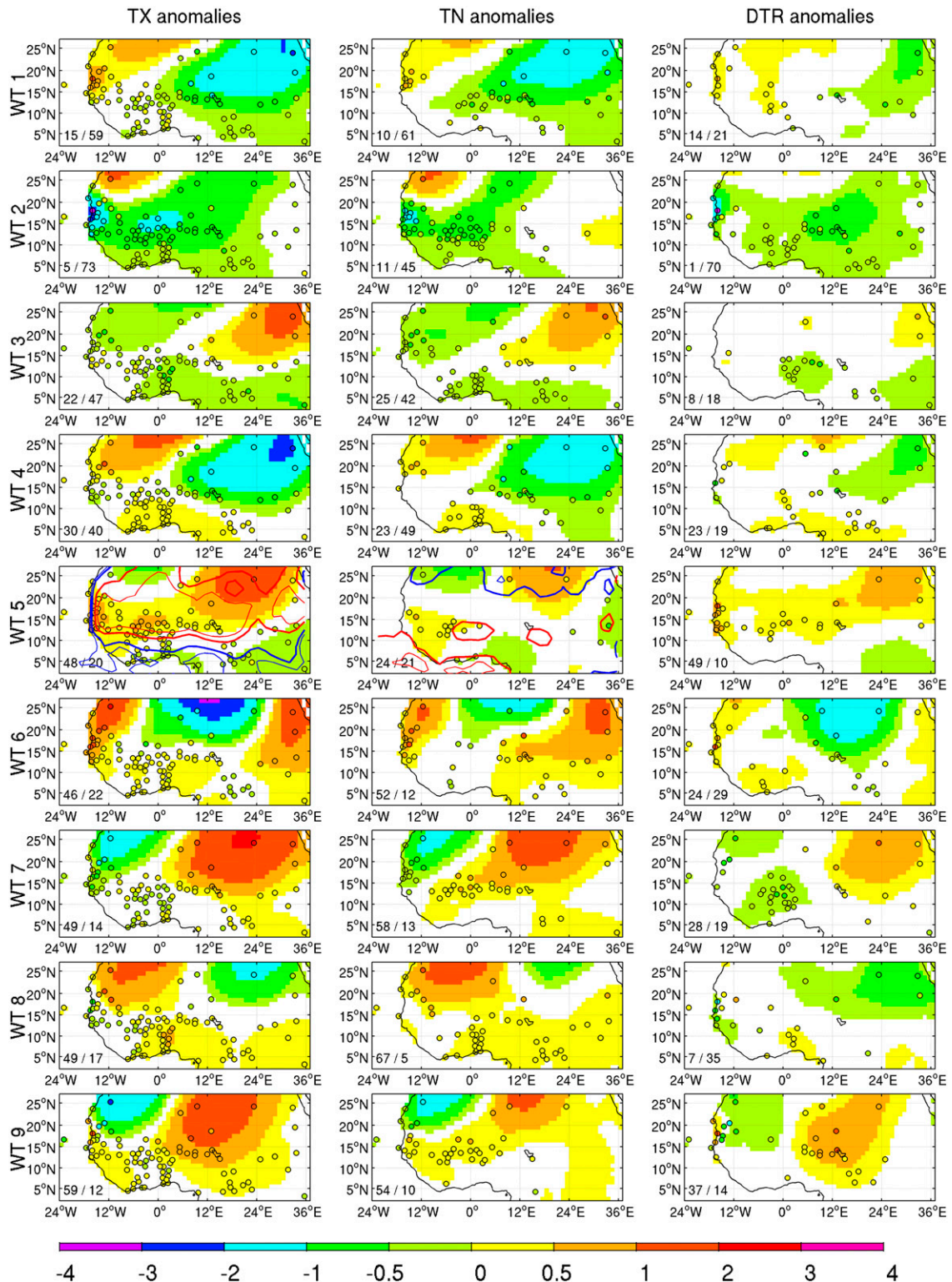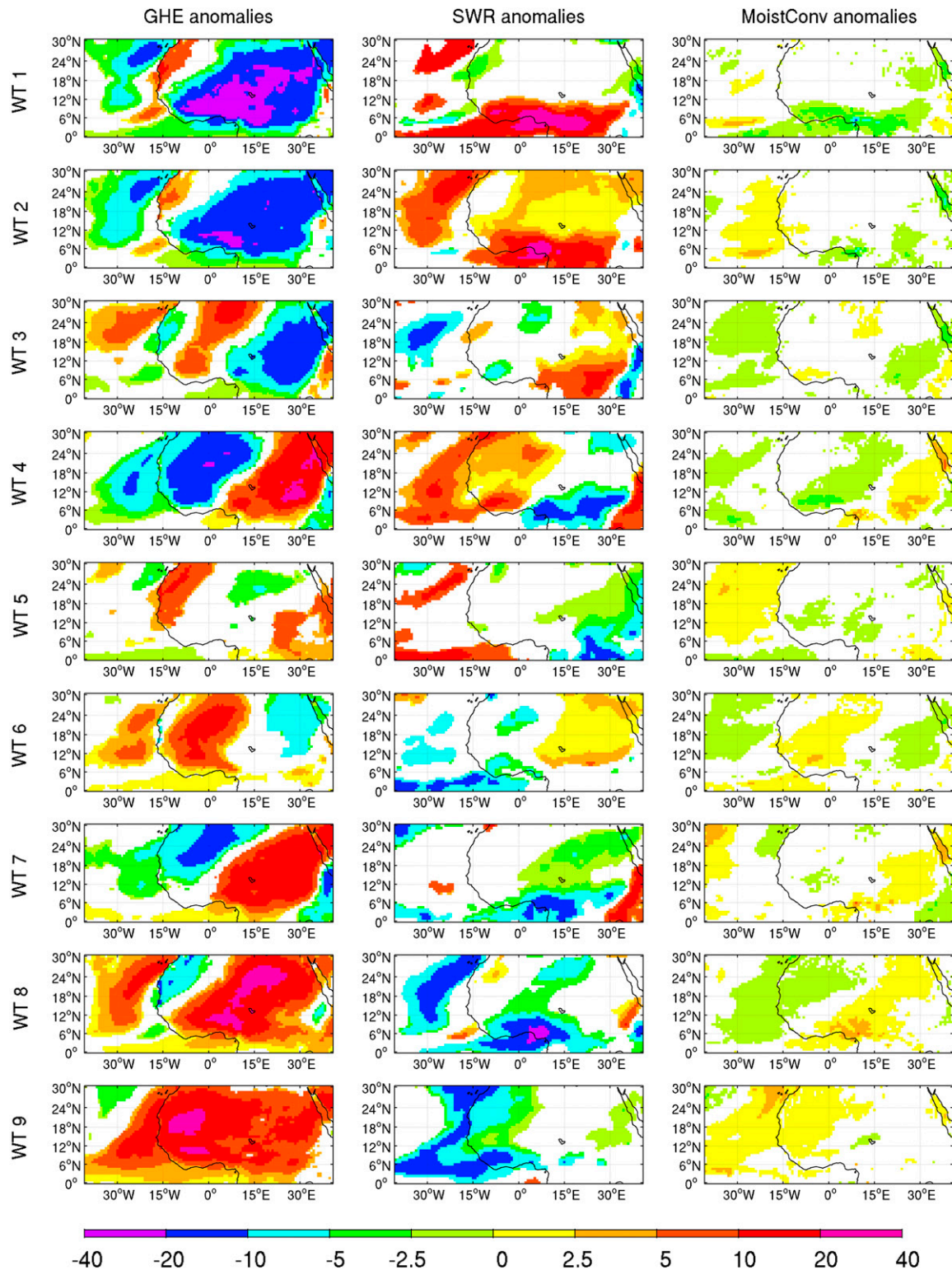
FIG. 11. As in Fig. 10, but for AMJ.

FIG. 12. Mean (left) surface greenhouse effect ($W\,m^{-2}$), (center) surface net shortwave radiation ($W\,m^{-2}$), and (right) vertically integrated moisture convergence ($mm\,day^{-1}$) in ERA (shading) associated with the nine WTs during February–March. Only significant anomalies at the two-sided 95% level according to 1000 random reshufflings of WT time series are displayed.
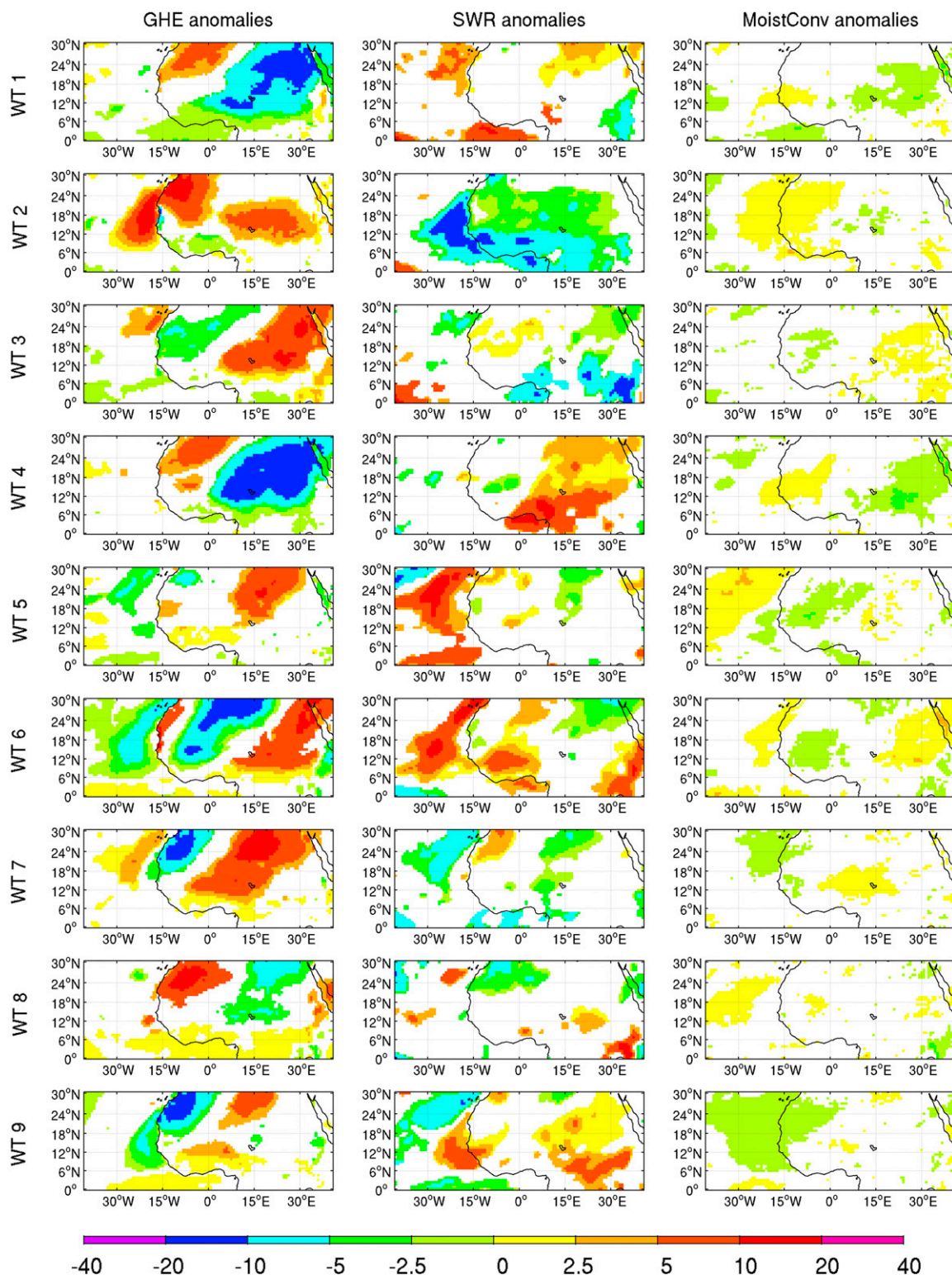
FIG. 13. As in Fig. 12, but for AMJ.

TABLE 1. Pattern correlations of TX and TN anomalies from Fig. 10 (from the Berkeley Earth dataset interpolated onto the ERA grid) and three terms of the energy budget (GHE, SWR, and MoistConv from ERA) from Fig. 12 for the nine WTs in FM.

WT	TX–GHE	TN–GHE	TX–SWR	TN–SWR	TX–MoistConv	TN–MoistConv
1	0.54	0.78	0.40	−0.04	−0.35	0.04
2	0.69	0.82	0.39	0.06	−0.13	0.05
3	0.78	0.91	−0.13	−0.46	0.21	0.40
4	0.77	0.92	−0.12	−0.48	0.28	0.39
5	0.60	0.79	0.39	0.03	−0.16	0.01
6	0.69	0.70	−0.18	−0.39	0.28	0.24
7	0.80	0.92	−0.09	−0.41	0.22	0.36
8	0.77	0.87	0.10	−0.21	0.28	0.32
9	0.19	0.44	0.68	0.38	−0.21	0.07

this WT, the pattern correlations are indeed higher between the TX/TN and SWR anomalies.

c. Relationships between WT and temperature/ thermodynamic processes in April–June

In AMJ (Fig. 11), the conclusions basically are unchanged. The main difference is that significant TX/TN anomalies usually cover a smaller area (as indicated in the bottom-left corner of each panel in Fig. 11) than in FM, consistent with the smaller scales represented by WT in the boreal spring than those in the late winter. This means that the statistical dependency of the TX/TN anomalies on the WT occurrence is weaker than in FM, beyond the fact that the amplitude of the TX/TN anomalies is also weaker in AMJ than in FM. The negative TX/TN anomalies are still observed mostly east and south of the anticyclonic anomalies in association with anomalous northerly flow. Thus, the air coming from the coolest regions (i.e., the Sahara north of 20°N for TN, northern Africa, the Atlantic Ocean and Guinean Africa for TX; see the climatological TX and TN means in the WT 5 panels of Fig. 11) tends to cool the regions crossed, while a warming is usually observed for the air coming from the warmest regions (i.e., the

equatorial Atlantic for TN and a broad belt between 10° and 26°N for TX; see the climatological TX and TN means in the WT 5 panels of Fig. 11). Nevertheless, this effect from the lateral advection of air is weaker in AMJ than in FM, since the spatial thermal gradients across tropical North Africa are strongly reduced in AMJ, especially for TN (Fig. 11). The positive TX/TN anomalies are usually located east of cyclonic anomalies in the anomalous southerly or westerly flow, conveying larger amounts of moisture than usual from the nearby tropical or equatorial Atlantic (Figs. 4 and 11). So, even in the boreal spring, northerly anomalies originating from or crossing the Sahara are usually related to negative TX/TN anomalies. There are some exceptions, as in WT 9 (Fig. 11), where northerly anomalies over the western Sahel (Fig. 4i) are related to weak positive TX/TN anomalies. As in FM, there is a very strong link between the TX/TN and GHE anomalies (Fig. 13; Table 2). The spatial correlations between the TX/TN and SWR anomalies are far weaker, except for SWR with TN in WT 5 and WT 7 (Table 2). The relationship between the GHE and MoistConv anomalies is robust in some WTs, with pattern correlations of 0.53, 0.55, 0.66, 0.5, and 0.58 for WTs 1, 3, 6, 7, and 9, respectively.

TABLE 2. Pattern correlations of TX and TN anomalies from Fig. 11 (from the Berkeley Earth dataset interpolated onto the ERA grid) and three terms of the energy budget (GHE, SWR, and MoistConv from ERA) from Fig. 13 for the nine WTs in AMJ.

WT	TX–GHE	TN–GHE	TX–SWR	TN–SWR	TX–MoistConv	TN–MoistConv
1	0.87	0.92	−0.11	−0.32	0.36	0.36
2	0.65	0.78	0.32	0.09	0.22	0.01
3	0.71	0.87	0.17	−0.20	0.10	0.35
4	0.83	0.89	−0.08	−0.28	0.15	0.24
5	0.83	0.91	−0.27	−0.47	0.04	0.09
6	0.77	0.90	−0.03	−0.39	0.35	0.47
7	0.88	0.94	−0.32	−0.52	0.26	0.34
8	0.76	0.88	−0.13	−0.38	0.19	0.25
9	0.88	0.94	0.13	−0.07	0.54	0.47

5. WT reconstruction of TX/TN anomalies

a. Introduction

The relevance of the information conveyed by the sequences of the WTs is analyzed through 1) the reconstruction of the interannual TX/TN seasonal anomalies on the basis of the WT occurrence and 2) the WT modulation in the occurrence of heat peaks (defined as the crossing of the 90th percentile of TX or TN). This section looks at the contribution of WT sequences to the TX/TN variations, assuming that the main thermal signal (i.e., the regional-scale fingerprint of global warming; Moron et al. 2016b) may not be closely related to the interannual variations of seasonal frequency of each WT. Our goal is also to look at the potential predictability (in the perfect prognosis sense, i.e., the assignment of each day to a given WT that is known a priori) of mean and extreme TX/TN anomalies associated with the WT occurrence.

b. Interannual variations of seasonal means

The first approach is an attempt to reconstruct the seasonal TX/TN anomalies from the daily WT sequences alone. This reconstruction is similar to the "flow analog" approach of Yiou et al. (2007) and Cattiaux et al. (2010). The best analog of a given target day is simply the one that minimizes its Euclidean distance with the target day in terms of atmospheric pattern anomalies (termed "flow"). Yiou et al. (2007) simply sampled n flow analogs among training seasons and considered the "analog" temperature or rainfall anomaly as the median of the anomalies of the n analogs. This approach is adapted here by randomly selecting, for each day of any FM and AMJ season, one WT that is identical to the one observed during the target day (referred to as a "WT analog" hereinafter) among the remaining seasons. A single day is sampled so as not to bias the interannual variance of seasonal averages (which is lowered as soon as the median or mean of a set of WT-analog days is selected), but this is repeated 100 times to estimate the correlation between the observed and reconstructed TX and TN seasonal anomalies from the daily WT sequence.

It is striking that the standard deviation is greatly reduced in FM and AMJ in the WT-analog approach (Fig. 14). This is partly related to the fact that the WTs do not explain the long-term warming trend, but also to the cancellation between the WTs occurring during a given season. In other words, WTs leading to anomalous positive TX/TN at local scale are roughly balanced by other WTs associated with anomalous negative TX/TN during a given season. This cancellation is especially marked for TN in AMJ since the spatially averaged ratio between the

observed and WT-analog interannual standard deviations is 2.5 (vs 2.2–2.3 for TX/TN in FM and TX in AMJ).

The correlation coefficients between the WT analog and the observed seasonal TX/TN anomalies are large north of 10°N, except over a southwest–northeast axis around 5°W, in FM (Fig. 15), where the mean TX and TN anomalies are frequently close to zero across the WT (Fig. 10). This decrease may thus be related to frequent transitions between an Atlantic and a continental domain in the nine WTs (Fig. 10; see section 4a), with the southwest–northeast gradient reflecting the primary impact of anticyclonic/cyclonic anomalies on TX/TN anomaly patterns. A residual warm or cold seasonal anomaly is conveyed by the whole WT sequence in FM, whereas the WT-analog seasonal anomalies are close to zero in AMJ (Fig. 15), except for localized regions over the western and eastern-central Sahara/Sahel north of 15°N. The zero, or even negative, skill in AMJ over most of the domain can be explained by the near cancellation between anomalously warm and cold WTs during a given season, but also by the small amplitude of the TX/TN anomalies associated with the WTs.

The WT-analog approach and reconstruction of seasonal TX/TN anomalies are repeated again for other clusterings corresponding to significant peaks in CI, as revealed by Figs. 2a and 2b, which are $k = 2, 3$, and 7 clusters in FM and $k = 2, 3, 5$, and 6 clusters in AMJ. Two scores are computed (Tables 3 and 4): 1) the pattern correlations between the Berkeley Earth maps in Figs. 15e–h and similar ones obtained with the other clusterings (not shown) and 2) the surface area covered by significant positive correlations, similar to Figs. 15e–h. Table 3 indicates that the reconstructions are similar among the clusterings; that is, the WT reconstructions of the TX/TN seasonal anomalies are mostly insensitive to the number of clusters. It is slightly more sensitive in AMJ (Table 4). This result is expected since the WT clustering is less robust (i.e., more days are unclassified because of a discrepancy between ERA and R2) and significant TX/TN anomalies associated with each WT cover a smaller area in AMJ (Fig. 11) than in FM (Fig. 10). The largest discrepancies against the nine-cluster solution analyzed through the paper are observed with the two-cluster solution (Table 4) but this clustering is almost unable to reproduce the interannual variations of the TX and TN seasonal anomalies. The other solutions with three, five, and six clusters are more similar to the nine-cluster solution (Table 4).

c. Occurrence of heat peaks

The second illustration of the usefulness of the WT approach consists of characterizing its ability to detect instantaneous heat peaks at the regional scale. The heat peaks are defined as the crossing of the 90th percentile
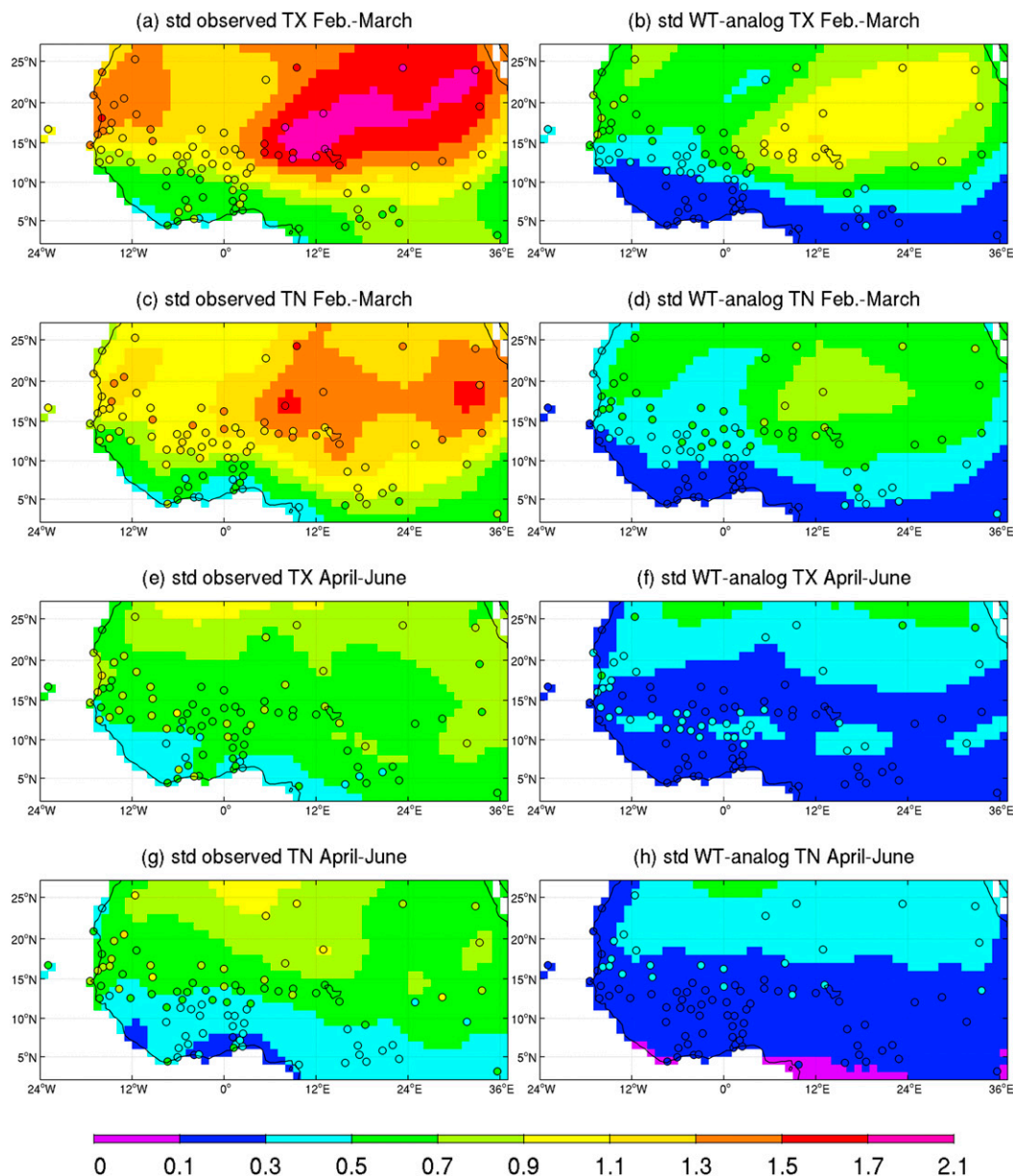
FIG. 14. Standard deviation (°C) of interannual (left) observed and (right) WT-analog TX and TN during (a)–(d) FM and (e)–(h) AMJ.

of TX or TN (computed on running 5-day intervals) at regional scales. Six areas are defined over the coastal Sahara and Sahel, central Sahel, eastern Sahel, central Sudan, and Guinea, and a heat peak is only reached when at least 50% of the grid points (or stations) exceed the local-scale 90th percentile of TX or TN. The modulation of the occurrence of heat peaks due to WTs is compared with 1000 random simulations in which WT sequences are randomly resampled. Figure 16 shows that the occurrences of heat peaks are significantly modulated by many WTs in FM, but also in AMJ, even if

the probabilities are usually lower. It is also clear that the mean TX/TN anomalies (Figs. 10 and 11) do not strictly reflect the anomalous occurrence of heat peaks (Fig. 16). For instance, the probability of heat peaks in FM is higher in WT 2 than in WT 1 in coastal Sahel (Fig. 16) while the mean TX/TN anomalies are roughly similar (Fig. 10). The anomalous positive probability of heat peaks is widespread in WT 9, except along the coast (Fig. 16). In AMJ, the number of WTs leading to significant anomalous probability of heat peaks is smaller than in FM (at least four WTs; Fig. 16). This result
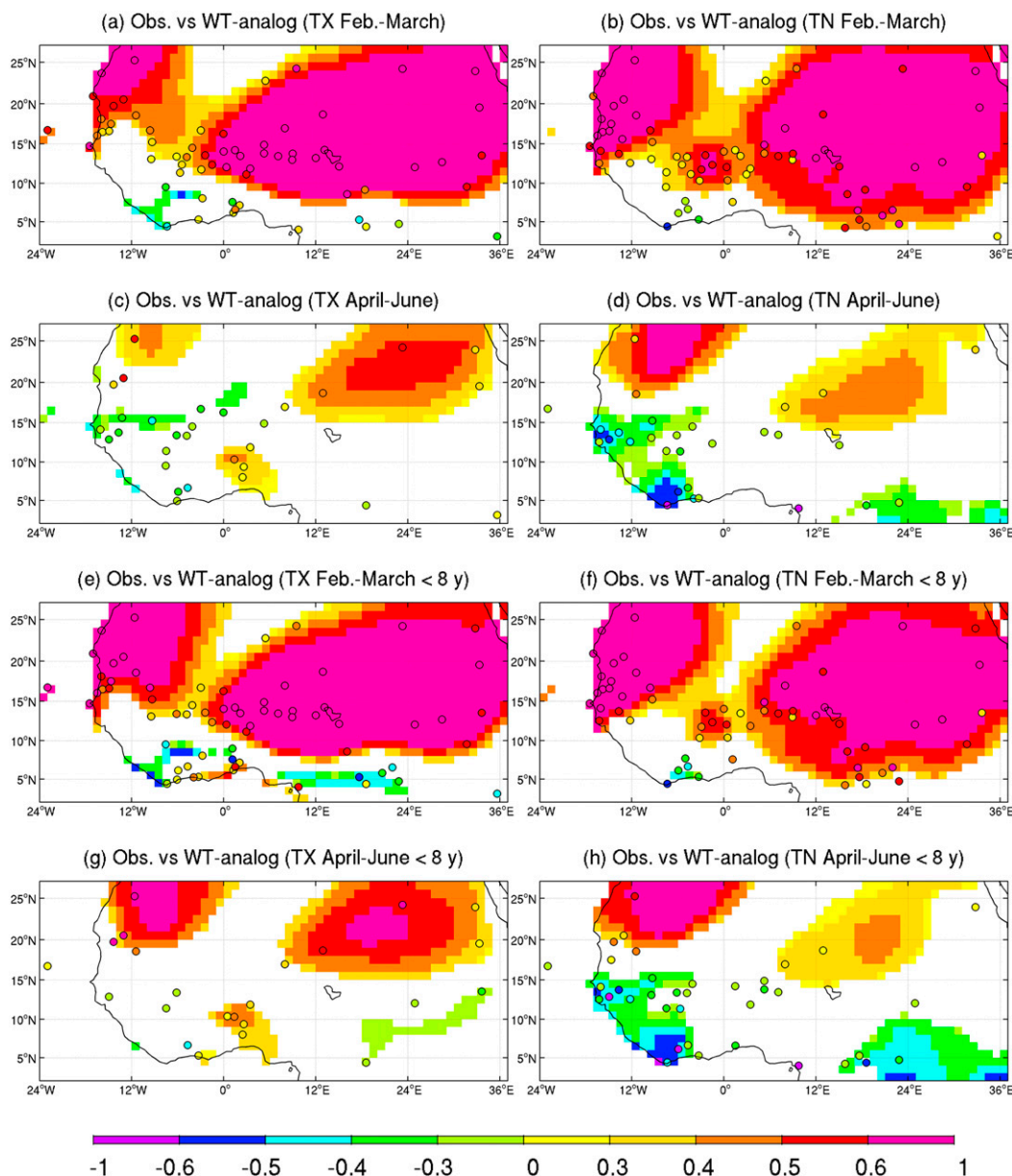
FIG. 15. Correlation between observed seasonal TX and TN anomalies and WT-analog (i.e., one WT that is identical to the one observed during the target day randomly chosen among the remaining seasons) reconstructed seasonal TX and TN anomalies for (a)–(d) raw values and (e)–(h) high-pass (≤ 8 yr) values. Only significant correlations at the two-sided 95% level according to a random phase that is based on 1000 time series having the same spectral power as the original time series but random phase (Janicot et al. 1996; Ebisuzaki 1997).

suggests that WT occurrence may be used to anticipate heat peaks at intraseasonal and synoptic time scales.

6. Summary and conclusions

The main purpose of this study has been to look at the modulation of TX/TN anomalies by means of regional-scale weather types during February–June, when both

the mean and extreme temperatures reach their highest annual peaks across tropical North Africa, south of the Sahara Desert (Guichard et al. 2009; Moron et al. 2016b; Barbier et al. 2018). The clustering of the daily SLP and low-level 925-hPa wind anomalies is separately applied over the end of the boreal late winter (February–March) and spring (April–June) to consider the slow seasonal changes in the mean atmospheric state (Fig. 1). These

TABLE 3. Pattern correlations (PC vs the nine-cluster solution shown in the main text) of TX and TN (from the Berkeley Earth dataset) skill maps and surface of significant positive correlations (surface in percent of total area) for different clusterings in FM.

	Two clusters	Three clusters	Seven clusters	Nine clusters
TX PC	0.87	0.97	0.97	1
TN PC	0.69	0.93	0.94	1
TX surface	56	63	62	71
TN surface	62	65	67	77

slow seasonal changes include the establishment and intensification of the African heat low and the slowdown of the extratropical westerlies along the northern edge of the domain. The main heating of the atmosphere associated with the deep convection in the ITCZ remains over the south of the domain (Guinean latitudes), even in June. The southern location of the main atmospheric heat source may have a major consequence, that is, the weak physical dependency between the near-equatorial and extratropical latitudes during this season. The weather types are extracted from a concatenation of two reanalyses (i.e., NCEP–DOE and ERA-Interim), allowing us to discriminate robust WTs—that is, those attributed to the same cluster in both reanalyses (86% of the days in FM and 78% of the days in AMJ)—from the remaining days, which are assigned to different WTs in ERA and R2 and thus represent indistinct atmospheric states that are not well represented by the WTs. In other words, considering two different reanalyses together is an empirical and a posteriori approach by which to classify days in a more robust way than when a single dataset is used.

The nine WTs (Figs. 3, 4, 8, and 9) may be interpreted as snapshots of traveling Rossby waves over the northern edge of the domain, or quasi-stationary and traveling MJO and Kelvin waves in the equatorial zone, or a combination of both phenomena. This interpretation is different from the situation in the extratropics in winter, where the WTs may be viewed as the dynamic attractors of atmospheric circulation, which are intrinsic topological features of the atmosphere's phase space (Ghil and Robertson 2002). The attempt to define the zonal and blocked atmospheric regimes at the hemispheric scale is an example of such a dynamic interpretation of the WTs

(or weather "regimes"). In our case of a tropical/subtropical area during the boreal late winter and spring, the WTs may be interpreted rather as coarse-grained statistical patterns, encapsulating the influence of different multiscale tropical and extratropical phenomena (as extratropical Rossby waves, dynamical weather regimes, the MJO, coupled convective equatorial waves, etc.). This statistical interpretation is still useful whenever the WTs discriminate significantly other climatic variables that are not included in their definition (TX and TN here). In that context, finding the "true" (if any) number of WTs is less critical than in a dynamic perspective, in which the number of clusters may be viewed as an empirical estimate of the dimension of the attractor. Consideration of a larger number of clusters will, for example, extract different snapshots of the same wave (or a combination of different waves) that are partly or fully included in a single WT when fewer clusters are used. It has been shown that phases of the NAO and the MJO significantly modulate most of the WTs (Figs. 6 and 7). The horizontal scale of negative SLP anomalies is slightly smaller in AMJ than in FM, and the modulation provided by the NAO is logically stronger in FM than in AMJ (Fig. 6). The modulation provided by the MJO is equally present in FM and AMJ, however. This connection between the "short time" scale of the WTs and the "intermediate" scale of the NAO and the MJO is worth considering for interpreting and potentially refining seamless predictions, which is a direct application of this approach, and is another proof of its usefulness, being able to "deconstruct" either operational medium-range or seasonal forecasts into occurrences or probability of occurrences of WTs. The WT framework can then be useful for short- and

TABLE 4. As in Table 3, but in AMJ.

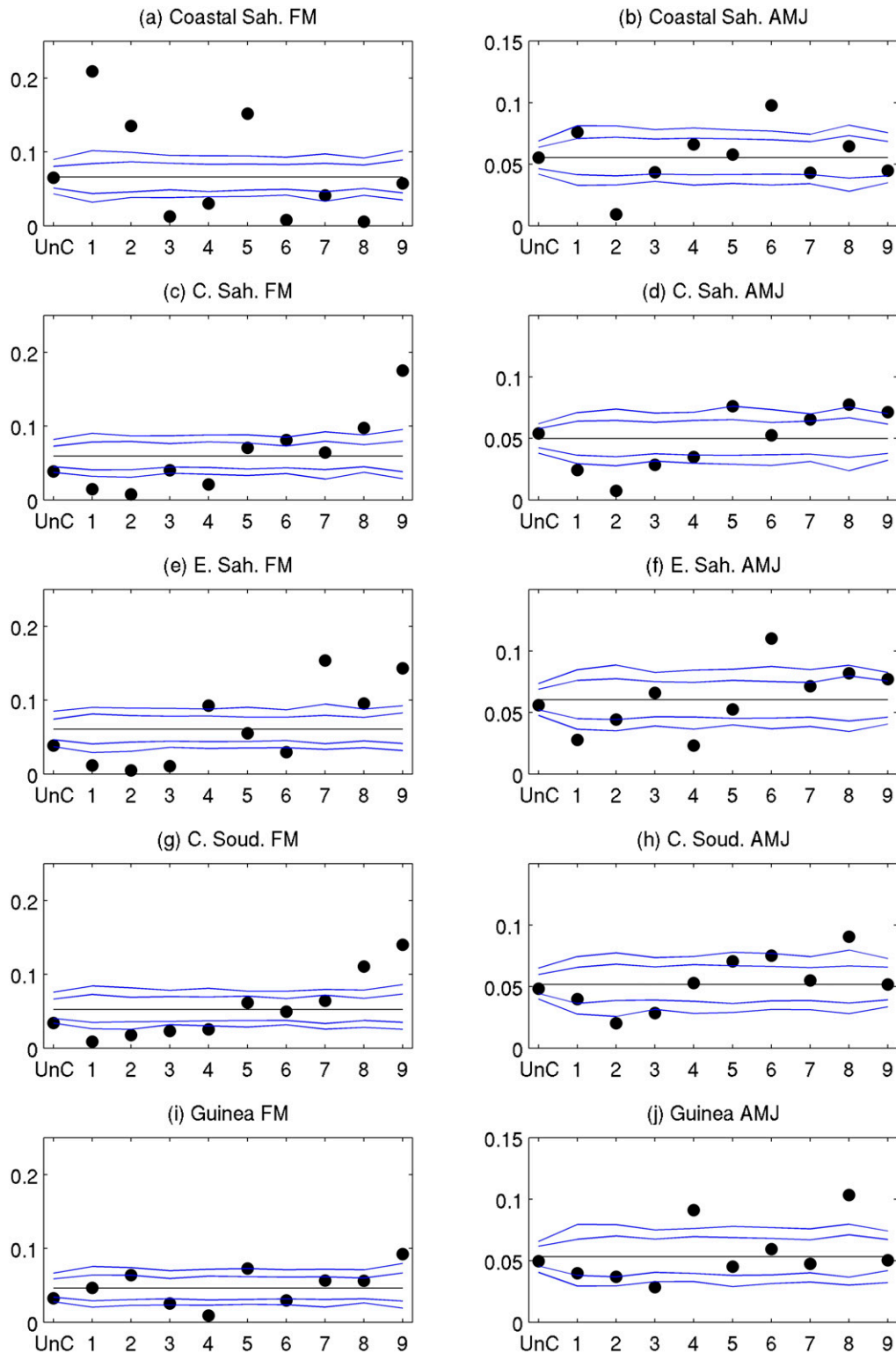|	Two clusters	Three clusters	Five clusters	Six clusters	Nine clusters
TX PC	0.28	0.73	0.79	0.92	1
TN PC	0.58	0.86	0.88	0.91	1
TX surface	0	10	19	31	31
TN surface	0	9	11	25	21

FIG. 16. Probability of occurrence (filled circles) of a heat peak defined as at least 50% of grid points (in the Berkeley Earth dataset) crossing the 90th percentile either in TX or TN according to each WT (the first value is for unclassified days; i.e., the WT is different between the R2 and ERA reanalyses). The 90th percentile is computed for running 5-day windows, and the five sectors are (a),(b) coastal Sahel west of 15°W and 13°–22°N; (c),(d) central Sahel, 8°W–8°E, 12°–17°N; (e),(f) eastern Sahel, 22°–38°E, 12°–17°N; and (g),(h) central Sudan, 8°W–8°E, 9°–12°N, and Guinea, 8°W–8°E, 4°–9°N. The blue lines indicate the 90% and 99% confidence bounds on the basis of 1000 random resamplings of WT sequences, and the black horizontal line is the mean probability of occurrence of a heat peak.

medium-term forecasts since it is trivial to assign any daily forecast to the WTs analyzed in this study, whenever the input variables are available.

The mean TX/TN anomalies associated with the robust WTs in either FM or AMJ show a similar pattern across the WTs: significant warm anomalies are mostly located east of cyclonic anomalies and significant cold anomalies are mostly located east of anticyclonic anomalies. The significance of TX and TN anomalies decreases usually toward the Guinean latitudes and the equator, suggesting that a dominant role is being played by WTs defined on a subtropical and tropical area. In FM, widespread cold and warm anomalies are mostly related to large-scale anticyclonic and cyclonic anomalies, respectively. The analysis of the main radiative fluxes suggests that the impact of WT on TX/TN anomalies is mostly driven by the greenhouse effect (Figs. 12 and 13). Westerly or southerly anomalies tend to advect moisture and thus to increase both TN and TX. This effect is superimposed on the lateral advection associated with air coming from warmer or cooler regions. The influence of downward shortwave radiation in the expected sense (i.e., warm TX anomalies with fewer clouds) is restricted to just a few WTs in FM.

The reconstruction of TX/TN anomalies by the WT sequences is analyzed using a resampling scheme that is based exclusively on the WT occurrences. It is shown that the standard deviation of the interannual TX/TN seasonal anomalies is underestimated by the WT reconstruction, especially for TN in AMJ (Fig. 14). This result can be explained by at least two phenomena: first, interannual variations of the WT seasonal frequencies do not properly explain the long-term warming trend and, second, there are antagonistic effects between anomalously warm and cold WTs, especially in AMJ. In other words, the anomalous frequency of a WT leading to warm anomalies is roughly canceled out by an anomalous frequency of a WT leading to cold anomalies at the intraseasonal time scale. This means that the WT occurrence mostly modulates the intraseasonal variability of TX/TN anomalies, whereas its weight on the interannual variability is only moderate in FM, especially north of 10°N, and is almost zero in AMJ, except for pockets in the Saharan and Sahelian belts. This partial inability to represent the interannual variations of seasonal TX/TN anomalies, at least in AMJ, does not prevent the WTs from significantly modulating the occurrence of heat peaks (defined here as at least 50% of stations at the regional scale crossing the local-scale 90th percentile of either TX or TN) in both seasons and even in areas where the mean TX/TN anomalies associated with the WTs are weak and usually nonsignificant (as over Guinean Africa). From a predictability point of view, this suggests that the WT occurrences may be a valuable predictor of near local-scale TX/TN anomalies on the intraseasonal time scale.

REFERENCES

Barbier, J., F. Guichard, D. Bouniol, F. Couvreux, and R. Roehrig, 2018: Detection of intraseasonal large-scale heat waves: Characteristics and historical trends during the Sahelian spring. *J. Climate*, **31**, 61–80, https://doi.org/10.1175/JCLI-D-17-0244.1.

Blackmon, M., Y. Lee, and J. Wallace, 1984a: Horizontal structure of 500 mb height fluctuations with long, intermediate and short time scales. *J. Atmos. Sci.*, **41**, 961–979, https://doi.org/10.1175/1520-0469(1984)041<0961:HSOMHF>2.0.CO;2.

——, ——, and ——, 1984b: Time variations of 500 mb height fluctuations with long, intermediate and short time scales as deduced from lag-correlation statistics. *J. Atmos. Sci.*, **41**, 981–991, https://doi.org/10.1175/1520-0469(1984)041<0981:TVOMHF>2.0.CO;2.

Cassou, C., 2008: Intraseasonal interaction between the Madden–Julian oscillation and the North Atlantic oscillation. *Nature*, **455**, 523–527, https://doi.org/10.1038/nature07286.

——, L. Terray, J. Hurrell, and C. Deser, 2004: Atlantic winter climate regime: Spatial asymmetry, stationarity with time and oceanic forcing. *J. Climate*, **17**, 1055–1068, https://doi.org/10.1175/1520-0442(2004)017<1055:NAWCRS>2.0.CO;2.

——, ——, and A. S. Phillips, 2005: Tropical Atlantic influence on European heat waves. *J. Climate*, **18**, 2805–2811, https://doi.org/10.1175/JCLI3506.1.

Cattiaux, J., R. Vautard, C. Cassou, P. Yiou, V. Masson-Delmotte, and F. Codron, 2010: Winter 2010 in Europe: A cold extreme in a warming climate. *Geophys. Res. Lett.*, **37**, L20704, https://doi.org/10.1029/2010GL044613.

Chauvin, F., R. Roehrig, and J.-P. Lafore, 2010: Intraseasonal variability of the Saharan heat low and its link with midlatitudes. *J. Climate*, **23**, 2544–2561, https://doi.org/10.1175/2010JCLI3093.1.

Cheng, X., and J. M. Wallace, 1993: Cluster analysis of the Northern Hemisphere wintertime 500-hPa height field: Spatial patterns. *J. Atmos. Sci.*, **50**, 2674–2696, https://doi.org/10.1175/1520-0469(1993)050<2674:CAOTNH>2.0.CO;2.

Cook, K. H., and E. K. Vizy, 2015: Detection and analysis of an amplified warming of the Sahara Desert. *J. Climate*, **28**, 6560–6580, https://doi.org/10.1175/JCLI-D-14-00230.1.

Dee, D., and Coauthors, 2011: The ERA-Interim reanalysis: Configuration and performance of the data analysis system. *Quart. J. Meteo. Soc.*, **137**, 553–597, https://doi.org/10.1002/qj.828.

Ebisuzaki, W., 1997: A method to estimate statistical significance of a correlation when data are serially correlated. *J. Climate*, **10**, 2147–2153, https://doi.org/10.1175/1520-0442(1997)010<2147:AMTETS>2.0.CO;2.

Fauchereau, N., B. Pohl, C. J. C. Reason, M. Rouault, and Y. Richard, 2009: Recurrent daily OLR patterns in the southern Africa/southwest Indian Ocean region, implications for South African rainfall and teleconnections. *Climate Dyn.*, **32**, 575–591, https://doi.org/10.1007/s00382-008-0426-2.

Fereday, D., J. Knight, A. Scaife, C. Folland, and A. Philipp, 2008: Cluster analysis of North Atlantic–European circulation types and links with tropical Pacific sea surface temperatures. *J. Climate*, **21**, 3687–3703, https://doi.org/10.1175/2007JCLI1875.1.

Fontaine, B., S. Janicot, and P.-A. Monerie, 2013: Recent changes in air temperature, heat wave occurrences and atmospheric circulation in northern Africa. *J. Geophys. Res. Atmos.*, **118**, 8536–8552, https://doi.org/10.1002/jgrd.50667.

Ghil, M., and A. W. Robertson, 2002: "Waves" vs. "particles" in the atmosphere's phase space: A pathway to long-range forecasting. *Proc. Natl. Acad. Sci. USA*, **99**, 2493–2500, https://doi.org/10.1073/pnas.012580899.

Guichard, F., L. Kergoat, E. Mougin, F. Timouk, F. Baup, P. Hiernaux, and F. Lavenu, 2009: Surface thermodynamics and radiative budget in the Sahelian Gourma: Seasonal and diurnal cycles. *J. Hydrol.*, **375**, 161–177, https://doi.org/10.1016/j.jhydrol.2008.09.007.

Janicot, S., V. Moron, and B. Fontaine, 1996: Sahel drought and ENSO dynamics. *Geophys. Res. Lett.*, **23**, 515–518, https://doi.org/10.1029/96GL00246.

Kalnay, E., and Coauthors, 1996: The NCEP/NCAR 40-Year Reanalysis Project. *Bull. Amer. Meteor. Soc.*, **77**, 437–471, https://doi.org/10.1175/1520-0477(1996)077<0437:TNYRP>2.0.CO;2.

Kamsu-Tamo, P.-H., S. Janicot, D. Monkam, and A. Lenouo, 2014: Convective activity over the Guinean coast and central Africa during northern spring at synoptic and intra-seasonal timescales. *Climate Dyn.*, **43**, 3377–3401, https://doi.org/10.1007/s00382-014-2111-y.

Kanamitsu, M., and Coauthors, 2002: NCEP–DOE AMIP-II Reanalysis (R-2). *Bull. Amer. Meteor. Soc.*, **83**, 1631–1643, https://doi.org/10.1175/BAMS-83-11-1631.

Kiladis, G. N., M. C. Wheeler, P. T. Haertel, K. H. Straub, and P. E. Roundy, 2009: Convectively coupled equatorial waves. *Rev. Geophys.*, **47**, 2008RG000266, https://doi.org/10.1029/2008RG000266.

Lavaysse, C., 2015: Saharan desert warming. *Nat. Climate Change*, **5**, 807–808, https://doi.org/10.1038/nclimate2773.

——, C. Flamant, S. Janicot, D. J. Parker, J.-P. Lafore, B. Sultan, and J. Pelon, 2009: Seasonal evolution of the West African heat low: A climatological perspective. *Climate Dyn.*, **33**, 313–330, https://doi.org/10.1007/s00382-009-0553-4.

Madden, R., and P. Julian, 1994: Observations of the 40–50-day tropical oscillation—A review. *Mon. Wea. Rev.*, **122**, 814–837, https://doi.org/10.1175/1520-0493(1994)122<0814:OOTDTO>2.0.CO;2.

Mera, R., A. G. Laing, and F. Semazzi, 2014: Moisture variability and multiscale interactions during spring in West Africa. *Mon. Wea. Rev.*, **142**, 3178–3198, https://doi.org/10.1175/MWR-D-13-00175.1.

Michelangeli, R., R. Vautard, and B. Legras, 1995: Weather regimes: Recurrence and quasi-stationarity. *J. Atmos. Sci.*, **52**, 1237–1256, https://doi.org/10.1175/1520-0469(1995)052<1237:WRRAQS>2.0.CO;2.

Mo, K., and M. Ghil, 1988: Cluster analysis of multiple flow regimes. *J. Geophys. Res.*, **93**, 10 927–10 952, https://doi.org/10.1029/JD093iD09p10927.

Moron, V., and G. Plaut, 2003: The impact of El Niño–Southern Oscillation upon weather regimes over Europe and the North Atlantic during boreal winter. *Int. J. Climatol.*, **23**, 363–379, https://doi.org/10.1002/joc.890.

——, A. W. Robertson, M. N. Ward, and O. Ndiaye, 2008: Weather types and rainfall over Senegal. Part I: Observational analysis. *J. Climate*, **21**, 266–287, https://doi.org/10.1175/2007JCLI1601.1.

——, ——, J.-H. Qian, and M. Ghil, 2015: Weather types across the Maritime Continent: From the diurnal cycle to interannual variations. *Front. Environ. Sci.*, **2**, https://doi.org/10.3389/fenvs.2014.00065.

——, I. Gouirand, and M. Taylor, 2016a: Weather types across the Caribbean basin and their relationship with rainfall and sea surface temperature. *Climate Dyn.*, **47**, 601–621, https://doi.org/10.1007/s00382-015-2858-9.

——, B. Oueslati, B. Pohl, S. Rome, and S. Janicot, 2016b: Trends of mean temperatures and warm extremes in northern tropical Africa (1961–2014) from observed and PPCA-reconstructed time series. *J. Geophys. Res.*, **121**, 5298–5319, https://doi.org/10.1002/2015JD024303.

Nicholson, S. E., 2009: A revised picture of the structure of the "monsoon" and land ITCZ over West Africa. *Climate Dyn.*, **32**, 1155–1171, https://doi.org/10.1007/s00382-008-0514-3.

Oudim Aström, D., B. Forsberg, and J. Rocklöv, 2011: Heat wave impact on morbidity and mortality in the elderly population: A review of recent studies. *Maturitas*, **69**, 99–105, https://doi.org/10.1016/j.maturitas.2011.03.008.

Oueslati, B., B. Pohl, V. Moron, S. Rome, and S. Janicot, 2017: Characterization of heat waves in the Sahel and associated physical mechanisms. *J. Climate*, **30**, 3095–3115, https://doi.org/10.1175/JCLI-D-16-0432.1.

Pohl, B., P. Camberlin, and P. Roucou, 2005: Typology of pentad circulation anomalies over the eastern Africa–western Indian Ocean region, and their relationship with rainfall. *Climate Res.*, **29**, 111–127, https://doi.org/10.3354/cr029111.

Roller, C. D., J.-H. Qian, L. Agel, M. Barlow, and V. Moron, 2016: Winter weather regimes in the northeast United States. *J. Climate*, **29**, 2963–2980, https://doi.org/10.1175/JCLI-D-15-0274.1.

Stocker, T., and Coauthors, 2013: *Climate Change 2013: The Physical Science Basis.* Cambridge University Press, 1535 pp., https://doi.org/10.1017/CBO9781107415324.

Sultan, B., and S. Janicot, 2003: The West African monsoon dynamics. Part II: The "preonset" and "onset" of summer monsoon. *J. Climate*, **16**, 3407–3427, https://doi.org/10.1175/1520-0442(2003)016,3407:TWAMDP.2.0.CO;2.

Vautard, R., 1990: Multiple weather regimes over the North Atlantic: Analysis of precursors and successors. *Mon. Wea. Rev.*, **118**, 2056–2081, https://doi.org/10.1175/1520-0493(1990)118<2056:MWROTN>2.0.CO;2.

——, and B. Legras, 1988: On the source of midlatitude low-frequency variability. Part II: Nonlinear equilibration of weather regimes. *J. Atmos. Sci.*, **45**, 2845–2867, https://doi.org/10.1175/1520-0469(1988)045<2845:OTSOML>2.0.CO;2.

Wheeler, M. C., and H. H. Hendon, 2004: An all-season real-time multivariate MJO index: Development of an index for monitoring and prediction. *Mon. Wea. Rev.*, **132**, 1917–1932, https://doi.org/10.1175/1520-0493(2004)132<1917:AARMMI>2.0.CO;2.

Yiou, P., R. Vautard, P. Naveau, and C. Cassou, 2007: Inconsistency between atmospheric dynamics and temperatures during the exceptional 2006/2007 fall/winter and recent warming in Europe. *Geophys. Res. Lett.*, **34**, L21808, https://doi.org/10.1029/2007GL031981.

Zhang, C., 2005: Madden–Julian oscillation. *Rev. Geophys.*, **43**, 2004RG000158, https://doi.org/10.1029/2004RG000158.